Quantifying the Impact of SST Feedback Frequency on the Madden-Julian Oscillation Simulations

Yung-Yao Lan[1], Huang-Hsiung Hsu[1], and Wan-Ling Tseng[2]

[1]Research Center for Environmental Changes, Academia Sinica, Taipei 11529, Taiwan

[2]Ocean Center, National Taiwan University, Taipei 10617, Taiwan

Correspondence to: Huang-Hsiung Hsu (hhhsu@gate.sinica.edu.tw)

Abstract

This study uses the CAM5 coupled to a 1-d ocean model to investigate the effects of intraseasonal SST feedback frequency on the Madden-Julian Oscillation (MJO) simulation with intervals at 30 minutes, 1, 3, 6, 12, 18, 24, and 30 days. The large-scale nature of the MJO in simulations remains intact with decreasing feedback frequency, although becoming increasingly unrealistic in both structure and amplitude, until 1/30days when the intraseasonal fluctuations are overwhelmingly dominated by unorganized small-scale perturbations in both atmosphere and ocean, as well as at the atmosphere-ocean interface where heat and energy are rigorously exchanged. The main conclusion is less frequent the SST feedback, more unrealistic the simulations. Our results suggest that more spontaneous atmosphere-ocean interaction (e.g., ocean response once every time step to every three days in this study) with high vertical resolution in the ocean model is a key to the realistic simulation of the MJO and should be properly implemented in climate models.

1. Introduction

The Madden–Julian Oscillation (MJO) is a large-scale tropical circulation that propagates eastward from the tropical Indian Ocean (IO) to the western Pacific (WP) with a periodicity of 30–80 days (Madden and Julian, 1972). In the Indo-Pacific region, the MJO processes involve intraseasonal variability of sea surface temperature (SST) (Chang et al., 2019; DeMott et al., 2014, 2015; Jiang et al., 2015, 2020; Krishnamurti

et al., 1998; Li et al., 2014; Li et al., 2020a; Newman et al., 2009; Pei et al., 2018; Stan, 2018; Tseng et al., 2015). The tropical air–sea interaction, influenced by the upper ocean, plays a crucial role in determining MJO characteristics due to the high heat capacity of the upper ocean within the intraseasonal range, which acts as a significant heat source for atmospheric variability (Watterson 2002; Sobel and Gildor 2003; Maloney and Sobel 2004; Sobel et al. 2010; Liang and Du, 2022).

Analyzing the mechanism of the intraseasonal oscillation (ISO) reveals that heat fluxes play a critical role in the development of intraseasonal SST variability (Hong et al., 2017; Liang et al., 2018). As demonstrated in Fu et al. (2017), underestimation (overestimation) of the air–sea coupling's impact on MJO simulations occurs when it is weak (strong) in the intraseasonal SST variability. Simulation improvements in the eastward propagation and regulation of MJO periodicity in the coupled models can be attributed to several factors such as enhanced low-level convergence and convective instability to the east of convection, as well as enhanced latent heat fluxes (Savarin and Chen, 2022) and SST cooling to the west of convection (DeMott et al., 2014). SST gradients have been found to induce patterns of mass convergence and divergence within the marine boundary layer (MBL), initiating atmospheric convection (de Szoeke and Maloney, 2020; Lambaerts et al., 2020).

Several recent studies have made significant progress in understanding the impact of air–sea coupling on the MJO, particularly at sub-daily scales (e.g., DeMott et al., 2015; Kim et al., 2018; Seo et al., 2014; Voldoire et al., 2022; Zhao and Nasuno, 2020). However, there is relatively limited discussion on the effect of air–sea coupling from few days to within half of the MJO period. Several studies have investigated the impact of intraseasonal SST on the MJO by coupled or uncoupled models. (e.g., DeMott et al., 2014; Gao et al., 2020b; Klingaman, and Demott, 2020; Pariyar et al., 2023; Stan, 2018). Simulations using time-varying SSTs from coupled global climate model (CGCM) to

force the atmospheric general circulation model (AGCM) showed a reduced intraseasonal SST variability, leading to weakened air–sea heat fluxes and eastward propagation (DeMott et al., 2014; Gao et al., 2020b; Klingaman, and Demott, 2020; Pariyar et al., 2023). Moreover, the absence of few days variability in SST promotes the amplification of westward power associated with Rossby waves (Stan, 2018).

Incorporating two-way coupling between the ocean and atmosphere has been proved valuable for simulating and predicting intraseasonal variability (e.g., DeMott et al., 2014; Lan et al., 2022; Stan, 2018; Tseng et al., 2015, 2020). As demonstrated in recent studies (e.g., Ge et al. 2017, Lan et al., 2022, Shinoda et al. 2021, and Tseng et al. 2015, 2022), incorporating high vertical resolution near the ocean surface positively influences the accurate representation of intraseasonal SST variability and enhances the MJO prediction capabilities. However, how frequent is the coupling needed is still not fully understood, considering the fact that the ocean and atmosphere could evolve in distinct time scales. And, would the coupling frequency in numerical models influence the accuracy of the MJO simulation?

In this study, we aim to investigate the specific effects of oceanic feedback frequency (FF) through air–sea coupling on the atmospheric intraseasonal variability, using the National Center for Atmospheric Research (NCAR) Community Atmosphere Model 5.3 (CAM5.3) coupled with the single-column ocean model named Snow–Ice–Thermocline (SIT). The coupled model is referred to as CAM5–SIT. The SIT model, consisting of 41 vertical layers, enables the simulation of SST and upper-ocean temperature variations with high vertical resolution (Lan et al., 2022). We have demonstrated in previous studies that coupling the SIT significantly improved the MJO simulations in several AGCMs (Tseng et al. 2015, 2022, Lan et al. 2022). The ability of the SIT with extremely high-resolutions (i.e., 12 layers within the first 10.5 m) to well resolve the upper ocean warm layer and the cool skin of the ocean surface was identified

as the main reason for the improved simulations.

The structure of this paper is organized as follows. Section 2 introduces the model, data, methodology, and experiments employed in this study. The performance of the CAM5–SIT models in simulating the MJO is discussed in Section 3, while Section 4 focuses on the impact of different configurations of sub-seasonal SST feedback periodicity on MJO simulations. Finally, Section 5 presents the conclusions.

2. Data, model experiments, and methodology

2.1 Observational data

Observational data sets used in this study include precipitation from the Global Precipitation Climatology Project (GPCP, 1° resolution, 1997–2010; Adler et al., 2003), outgoing longwave radiation (OLR, 1° resolution, 1997–2010; Liebmann, 1996), and daily SST (optimum interpolated SST, OISST, 0.25° resolution, 1989–2010; Banzon et al., 2014) from the National Oceanic and Atmosphere Administration, and the fifth generation ECMWF reanalysis (ERA5), with a resolution of 0.25° for the period of 1989–2020 (Hersbach and Dee, 2016). Various variables from ERA5 were considered, including winds, vertical velocity, temperature, specific humidity, sea level pressure, geopotential height, latent and sensible heat, and shortwave and longwave radiation. For the initial conditions of the SIT, the SST data was obtained from the Hadley Centre Sea Ice and Sea Surface Temperature dataset version 1 (HadISST1), with a resolution of 1° for the period of 1982–2001 (Rayner et al., 2003). The ocean subsurface data, including climatological ocean temperature, salinity, and currents in 40 layers, were retrieved from the National Centers for Environmental Prediction (NCEP) Global Ocean Data Assimilation System (GODAS) with a resolution of 0.5° for the period of 1980–2012 (Behringer and Xue, 2004). These data were used for a weak nudging (Tseng et al. 2015 2022; Lan et al. 2022) in the SIT model.

2.2 Experimental design

In this study, we investigated the role of oceanic FF using coupled CAM5–SIT and atmosphere-only CAM5 (A–CTL). Previous studies (Lan et al., 2022; Tseng et al., 2022) have provided a detailed description of the every timestep coupling CAM5–SIT model and its performance in simulating the MJO. Table 1 displays the experimental configuration, incorporating monthly HadISST1 (uncoupled region) and ice concentrations over a 30-year period centered around the year 2000 (F2000 compsets, Rasch et al., 2019). Solar insolation, greenhouse gas and ozone concentrations, and aerosol emissions representative of present-day conditions were prescribed. In the A–CTL, observed monthly-mean SST around the year 2000 was prescribed to force the CAM5. For the coupled simulations, we adjusted the Flux Coupler (CPL) restriction in the Climate Earth System Model (CESM1; Hurrell et al., 2013) by implementing asymmetric exchange frequencies between the atmosphere and the ocean. The ocean continuously receives atmospheric forcing at every time step (30 minutes) and the temperature changes accordingly, but the SST seen by the atmospheric model is fixed at each timestep for a specified time span (e.g., 1, 3, 6, 12, 18, 24, and 30 days). That is, the SST seen by the atmospheric model only changed until the end of the specified time span.

Two sets of experiments in addition to the A–CTL were conducted, each representing a different SST feedback frequency:

(1) High-frequency SST feedback set: This set includes the control experiment (C–CTL) with SST feedback at every timestep (FF as 48/day), once a day (C–1day: FF as 1/day), and every 3 days (C–3days: FF as 1/3days).

(2) Low-frequency SST feedback set: This set includes experiments with SST feedback to the atmosphere for every 6 days (C–6days: FF as 1/6days), 12 days

(C–12days: FF as 1/12days), 18 days (C–18days: FF as 1/18days), 24 days (C–24days: FF as 1/24days), and 30 days (C–30days: FF as 1/30days).

The SIT is coupled to CAM5 between 30° N to 30° S. The ocean was weakly nudged (using a 30-day exponential time scale) between depths of 10.5 m and 107.8 m, and strongly nudged (using a 1-day exponential time scale) below 107.8 m, based on the climatological ocean temperature data from NCEP GODAS. No nudging was applied in the upper-most 10.5 meters, allowing the simulation of rigorous air–sea coupling near the ocean surface.

During the simulation, the SIT recalculated the SST within the tropical air–sea coupling region. Outside this coupling region, the annual cycle of HadSST1 was prescribed. No SST transition between the tropical air–sea coupling zone and the extratropical SST-prescribed regions was applied. The ocean bathymetry for the SIT was derived from the NOAA's 1 arc-minute global relief model of Earth's surface that integrated land topography and ocean bathymetry (ETOPO1) data (Amante and Eakins, 2009). To ensure consistency and comparability, all observational, atmospheric, oceanic, and reanalysis data were interpolated into a horizontal resolution of 1.9° × 2.5° for model initialization, nudging, and comparison of experimental simulations.

2.3 Methodology

The analysis focused on the boreal winter period (November–April), the season with the most pronounced eastward propagation of the MJO. To identify intraseasonal variability, the CLIVAR MJO Working Group diagnostics package (CLIVAR, 2009) and a 20–100-day filter (Wang et al., 2014) was used. MJO phases were defined based on the Real-time Multivariate MJO series 1 (RMM1) and series 2 (RMM2) proposed by Wheeler and Hendon (2004), which utilized the first two principal components of combined near-equatorial OLR and zonal winds at 850 and 200 hPa. The band-pass

filtered data were used to calculate the index and define the MJO phases.

Analysis of column-integrated MSE budgets was conducted to investigate the association between tropical convection and large-scale circulations. The column-integrated MSE budget equation (e.g., Sobel et al., 2014) is approximately given by

$$\langle\frac{\partial h}{\partial t}\rangle' = -\langle u\frac{\partial h}{\partial x}\rangle' - \langle v\frac{\partial h}{\partial y}\rangle' - \langle w\frac{\partial h}{\partial p}\rangle' + \langle LW\rangle' + \langle SW\rangle' + \langle SH\rangle' + \langle LH\rangle' \quad (1)$$

where h denotes the moist static energy

$$h = c_p T + gz + L_v q \quad (2)$$

where T is temperature (K); q is specific humidity (Kg Kg^{-1}); c_p is dry air heat capacity at constant pressure (1004 J K^{-1} kg^{-1}); L_v is latent heat of condensation (taken constant at 2.5 × 10^6 J kg^{-1}); u and v are horizontal and meridional wind (m s^{-1}), respectively; ω is the vertical pressure velocity (Pa s^{-1}); LW and SW are the longwave and shortwave radiation flux (W m^{-2}), respectively; and LH and SH are the latent and sensible surface heat flux (W m^{-2}), respectively. The angle bracket ($\langle * \rangle$) represents mass-weighted vertical integration from 1000 to 100 hPa; and the intraseasonal anomalies are represented as $\langle * \rangle'$.

3. Results

3.1 The mean state and intraseasonal variability of SST

The variability of SSTs plays a crucial role in the dynamics of the MJO. Studies based on observations from TOGA COARE and DYNAMO revealed that MJO events exhibited a stronger ocean temperature response compared to average conditions (de Szoeke et al., 2014). Wu et al. (2021) revealed the better MJO prediction skill in the CGCM could be contributed by the improved representation of high-frequency SST fluctuations related to the MJO, with warm (cold) SST anomalies to the east (west) of MJO convection, through the convection–SST feedback processes (Li et al., 2020a; Wu

et al., 2021). It is therefore necessary to check on the influences of coupling and coupling frequency on the SST fluctuations.

Table 2 presents the oceanic temperature anomalies for the DJF seasonal mean, including the differences in oceanic temperature between the SST and depths of 10m ($\overline{\Delta \boldsymbol{T}}_{\boldsymbol{0-10m}}$) and 30m ($\overline{\Delta \boldsymbol{T}}_{\boldsymbol{0-30m}}$), as well as 20–100 days maximum and minimum SST and oceanic temperature at 10m depth (T_{10m}). The region of 110–130° E and 5–15° S was selected because of the largest variation in the 20–100-day bandpass-filtered SST when the MJO passes over the Indo-Pacific region. Simulated DJF seasonal mean SST (300.8K to 302.0 K) are generally smaller than OISST (302.2 K) but increase with the lower SST feedback frequency except in C–30days (302.7 K), while the SST standard deviation remains within 0.8 K, smaller than OISST (0.96 K), except in C−24days (1.06 K) and C−30days (1.71 K) that implies the potential jump in SST.

The simulated subsurface (0–10m and 0–30m) ocean temperatures were compared with those in the NCEP GODAS reanalysis and presented as ($\overline{\Delta \boldsymbol{T}}_{\boldsymbol{0-10m}}$ and $\overline{\Delta \boldsymbol{T}}_{\boldsymbol{0-30m}}$). The $\overline{\Delta \boldsymbol{T}}_{\boldsymbol{0-10m}}$ in high-frequency experiments maintained 0.1 K temperature difference. In low-frequency experiments, $\overline{\Delta \boldsymbol{T}}_{\boldsymbol{0-10m}}$ increased from 0.2 to 1.0 K with decreasing SST feedback frequency. The temperature difference ($\overline{\Delta \boldsymbol{T}}_{\boldsymbol{0-30m}}$) in both high-frequency and low-frequency experiments remains approximately 0.8K, except for C–24days and C–30days with an increase as high as 1.4 K and 2.1 K, respectively, with larger standard deviations. The comparison revealed the cooling effect of the SIT on the seasonal mean SST, especially in the higher-frequency coupling experiment due to the more rigorous heat exchanges between ocean and atmosphere. However, in the lower frequency experiments, the SST became much warmer and so did vertical temperature differences due likely to the unrealistically large heat accumulation of loss in the ocean.

As for the MJO simulation, the SST fluctuation is more relevant. The OISST fluctuation through a MJO cycle was about $\pm$0.21 K. In comparison, the uncoupled A–

CTL, which was forced by monthly mean HadISST1, yielded a negligible SST fluctuation (-0.003–0.02 K) as expected. In the high-frequency experiments, SST fluctuated in magnitudes similar to that in the daily OISST. The amplitude became unrealistically larger in the low-frequency coupling experiments with C–30days reaching as high as 0.6 K. The increasingly larger amplitudes were likely resulted from the heat accumulation in the ocean because of less frequent feedback (or heat release) to the model atmosphere. Changes in coupling frequency led to different amplitudes of SST fluctuation in a MJO cycle. As will be revealed latter, this effect had marked influence on the MJO simulations.

3.2 MJO simulation: high-frequency and low-frequency SST feedback experiments

3.2.1 General structure

The propagation characteristics of the different experiments were analyzed using the wavenumber-frequency spectrum (W-FS). The spectra of unfiltered U850 in ERA5, A–CTL, and all coupling experiments with different feedback frequency are shown in Fig. 1a–j. The C–CTL experiment accurately captures the eastward propagating signals at zone wavenumber 1 with 30–80-day period (Fig. 1a and 1c), although with a slightly larger amplitude than ERA5 (Fig. 1a). By contrast, the uncoupled A–CTL produced an unrealistic spectral shift to time scales longer than 30–80 days (Fig. 1b) and simulated the unrealistic westward propagation at wavenumber 2.

The W-FS spectra of the C–1day and C–3day experiment show two peaks for zone wavenumber 1 over the 30 to 80-day period. The low-frequency experiments (i.e., from C–6days to C–30days) increasingly enhanced the amplitudes and lowered the frequency of intraseasonal perturbations with decreasing feedback frequency. Furthermore, unrealistic westward W-FS of U850 becomes evident in (Fig. 1h–i) in the

C–18days, C–24days, and C–30days experiments, reflecting the stationary nature of simulated MJO seen in Fig. 2i–j.

The Hovmöller diagrams in Fig. 2a–j depict the evolution of 10° N–10° S averaged precipitation and U850 anomalies on intraseasonal timescales, represented by the lagged correlation coefficients with the precipitation averaged over 10° S–5° N, 75–100° E. In GPCP/ERA5, observed precipitation and U850 propagated eastward from the eastern IO to the dateline, with precipitation leading U850 by approximately a quarter of a cycle and a propagation speed of about 5 m s^{-1} (Fig. 2a). The A–CTL simulation was dominated by stationary features, with westward-propagating tendency over the IO and weak and slow eastward propagation over the MC and WP (Fig. 2b). The Hovmöller diagrams derived from high-frequency and low-frequency experiments (Fig. 2c–h) display the key eastward propagation characteristics in both precipitation and U850, as well as the phase relationship between them, except in C–24days and C–30days that were dominated by stationary perturbations. Further decreased feedback frequency from 1/C–24days to 1/C–30days also further weakened the signals of precipitation and U850. More detailed discussion on this topic will be presented in the subsequent chapter.

We conducted a wavenumber-frequency power spectral analysis (Wheeler and Kiladis 1999) to examine the phase lag and coherence between the tropical circulation and convection. Figures 3a–i illustrate the symmetric part of OLR and U850 for NOAA/ERA5 data and all model experiments. The MJO band exhibits a high degree of coherence, indicating a strong correlation between NOAA MJO-related OLR signal and wavenumbers 1–3 (Fig. 3a). The phase lag in the 30–80-day band is approximately 90°, consistent with previous studies (Ren et al., 2019; Wheeler and Kiladis 1999). All model experiments simulated the coherence within wavenumber 3 in the MJO band, with a phase lag similar to NOAA/ERA5 data. However, the A–CTL spectrum exhibits

261 only half of the observed coherence peak at wavenumber 1, and also weaker coherence
262 at wavenumbers 2–3 for the 30–80-day period compared to NOAA/ERA5 data. The
263 experiments C–CTL, C–1day, C–3days, C–6days, C–12days, and C–18days yielded
264 wavenumber-1 coherence peak similar to that in NOAA/ERA5. Additionally, as the
265 SST feedback frequency decreases from 1/12days to 1/30days, the experiments
266 increasingly simulated unrealistic coherence in the very low frequency with a wide
267 range of zonal wavenumber from 1 to 12 (Fig. 3g–j), i.e., no zonal scale preference.
268 Figure 4 shows the phase–longitude diagrams in which the 20–100-day filtered
269 precipitation (shaded) and SST (contour) anomalies were averaged over 10° S to 10° N
270 to determine the relationship between precipitation and SST fluctuations and to provide
271 insights into the connection between air–sea coupling and convection. As expected, the
272 A–CTL did not simulate the eastward-propagating coupled SST-convection
273 perturbations as in observation (Fig. 4a), whereas C–CTL, C–1day, and C–3days
274 properly reproduced the observed features. The eastward-propagating coupled
275 perturbations were also simulated in C–6days, C–12days, and C–18days, but with
276 unrealistically increasing amplitudes near the dateline, especially in the C–18days
277 experiment. The perturbation amplification near the dateline was likely due to the lack
278 of ocean circulation in the CAM5–SIT. The amplification was also seen in C–24days
279 that failed to simulate the eastward-propagating intraseasonal perturbations. When
280 coupling frequency was reduced to 1/30days, the eastward propagation could no longer
281 be simulated and was replaced by unorganized standing oscillations in much smaller
282 zonal scales.
283 Liang et al. (2018) suggested that SST leading precipitation by 10 days implies
284 air–sea interactions at the intraseasonal timescale during MJO events, with SST playing
285 a crucial role in modulating the MJO's intensity and propagation. The A–CTL
286 simulation exhibited weak SST anomalies and stationary precipitation when using the

monthly average HadISST1. By contrast, the C–24days and C–30days experiment showed no clear phase lag between disorganized SST and precipitation perturbations. A comparison between simulation results and observation indicates that the air–sea interaction plays a crucial role in facilitating eastward propagation and higher frequency feedback yields more realistic simulations.

3.2.2 Vertical structures of the MJO in the atmosphere

Air–sea interaction plays a significant role in influencing atmospheric moisture and convection associated with the MJO (Savarin and Chen, 2022). Whereas the ocean to the east of deep convection warmed due to more downwelling shortwave radiation and less heat fluxes into the atmosphere associated with weaker winds, near-surface moisture convergence under the anomalous subsidence over the warmer water preconditioned the eastward movement of the deep convection (DeMott et al., 2015; Zhang, 2005). The MJO was noted to detour southward when crossing the MC region, exhibiting enhanced convective activity preferentially in the southern MC area and weaker convection in the central MC area (Hsu and Lee 2005, Wu and Hsu 2009, and Kim et al. 2017). Hovmöller diagrams in Fig. 5a–j illustrate the relationship between the vertical structure of air temperature (contoured, in K) and specific humidity (shading, in g kg^{-1}) anomalies from the surface to 200 hPa averaged over 5–20° S and 120–150° E. In ERA5, the lower-level positive temperature anomaly in phase 3 (i.e., preconditioning phase) leads the development of deep temperature and moisture anomalies (i.e., deep convection) after phase 4 over the MC, when moisture anomalies reached the maxima at 700–500 hPa. This two-phase upward development was not properly simulated in A–CTL, which shows sudden switch between positive and negative anomalies in the entire troposphere, instead of progressively upward development with time. The upward development was generally simulated in coupled

simulations from C–CTL to C–6days (Fig. 5c–e), although the negative temperature anomalies below 500 hPa were over-simulated after phase 5. It became less well simulated beyond C−12days and was gradually replaced by sudden phase switch as in the A−CTL, especially in C−30days (Fig. 5f–j). The preconditioning phase completely disappears in C–18 days and beyond. As identified in previous studies, the two-phase upward development is a manifestation of air−sea coupling. The missing of this coupling evidently resulted in the poor simulation in the A−CTL and extremely low feedback frequency experiments.

3.2.3 Vertical structures of the MJO in the ocean

The 1-D turbulence kinetic energy (TKE) ocean model incorporates a high vertical resolution that captures the vertical gradient of temperature in the upper ocean. Figure 6 (left column) illustrates the vertical structures of oceanic temperature between 0- and 60-meters during phase 2–3 when the deep convection occurred over the eastern IO (60–90° E) and easterly anomalies prevailed over the MC and western Pacific. In the high-frequency experiments (Fig. 6a, 6c, 6e), the upper oceanic temperatures exhibit warming patterns within 30 meters depth at 100–140° E (i.e., east of the deep convection and under the easterly anomalies), apparently due to more downwelling short wave radiation and less heat flux release to the atmosphere. By contrast, the cooling near the dateline was associated with westerly anomalies. With decreasing feedback frequency, the cooling to the east of 150°E seen in high frequency experiments was replaced by oceanic warming that amplified with further feedback frequency decrease. The warming region that became more widespread and larger amplitude with less frequent feedback eventually grew to cover the entire IO and WP, an area much larger than the scale of the atmospheric MJO. The mismatch between the atmospheric and oceanic anomalies suggested the weakening atmospheric-ocean coupling that

resulted in poor simulation of the MJO in the low frequency feedback simulations. The emergence of small-scale unorganized structures with decreasing feedback frequency is also evident in phase 4-5 (right column of Fig. 6), e.g., negative ocean temperature anomalies in the Indian Ocean under the prevailing westerly anomalies.

4. Discussion

4.1 Dynamic lead–lag relationship in intraseasonal variability

The lead–lag relationship refers to a situation where one variable (leading) is cross-correlated with the values of another variable (lagging) in subsequent phases, particularly in the case of SST fluctuations and MJO-related atmospheric variations between phase 1 and 8 within the domain of 110–130° E and 5–15° S (Fig. 7). The analyzed variables include 20–100-day filtered latent heat flux (LHF, indicated by green shading), OLR (indicated by a yellow bar chart), net surface solar radiation (FSNS, indicated by an orange bar chart), U850 (indicated by a purple bar chart), 30-meter depth oceanic temperature (30-m T multiplied by 100, indicated by a black line), and SST (multiplied by 10, indicated by an orange line). Positive value in LHF and FSNS represents an upward flux from ocean to atmosphere.

Decrease in LHF, which indicates a reduction in heat loss from the ocean, and negative FSNS, indicating that solar radiation is heating the ocean, coincide with easterly anomaly that contributes to positive SST anomaly in ERA5 (Fig. 7a). Reversed fluxes are associated with westerly anomalies. This lead–lag relationship depicts the in-situ atmospheric forcing on the oceanic variability during a MJO. As the MJO convection progresses through the region (110–130° E and 5–15° S), several changes in atmospheric and oceanic variables occur. These changes include a shift in OLR from positive to negative values, a decrease in SST, a transition to westerly winds, and an increase in positive FSNS and LHF (Fig. 7a). The temporal variations in SST anomaly

365 from C–CTL to C–12days were predominantly influenced by FSNS, with LHF playing
366 a secondary role, similar to the findings of Gao et al. (2020a). With the exception of
367 experiments of A–CTL, C–24days, and C–30days, both the high-frequency and low-
368 frequency SST feedback experiments simulated similar lead–lag relationships as in
369 ERA5 (Fig. 7c–h). In the C–24days and C–30days experiments, LHF was the largest
370 flux term (note the different vertical scale for the two experiments) whereas the wind,
371 OLR, and FSNS anomalies were much weaker than in other experiments. In the A–CTL
372 experiment, which was forced by monthly HasISST1 data, the SST anomalies were
373 small as expected, whereas fluxes although weak are still evident in response to
374 atmospheric perturbations (Fig. 7b). Conversely, in both C–24days and C–30days
375 experiments, a misalignment in the lead–lag relationship was observed, accompanied
376 by weak anomalies in OLR and FSNS. (Fig. 7i and 7j). This disparity between LHF and
377 wind was likely due to the unrealistically widespread and large oceanic warming as
378 shown in Fig. 6m and 6o.

379 In the simulations, the maximum positive anomaly in 30-m T was delayed by one
380 phase compared to SST, indicating the transfer of heat from the ocean surface into the
381 upper ocean progressively. Similarly, the occurrence of the most negative 30-m T
382 anomaly was also delayed by one phase compared to SST, revealing the buffering role
383 of the upper ocean when the atmospheric component of the MJO extracted (or deposited)
384 heat (energy) from (in) the ocean (Fig. 7c–i). This delayed effect was also evident in
385 the field campaign. de Szoeke et al. (2015) observed that the warmest 10-m ocean
386 temperature occurred a few days later than the peak temperature at 0.1 m. Additionally,
387 the 0.1-m ocean temperature was typically as warm as or warmer than the 10-m
388 temperature as seen in Fig. 6. In the extreme low frequency feedback experiments, the
389 amplitude of 30-m temperature became unrealistically large due likely to the continuous
390 accumulation or loss of the ocean heat.

391

392 **4.2 Unorganized perturbations in extreme frequency feedback scenarios**

393 DeMott et al. (2014) noted that in uncoupled experiments, the NCAR CAM
394 superparameterized version 3 (SPCAM3) exhibited strong eastward propagation when
395 5-day running mean SST was prescribed, but relatively weaker propagation for monthly
396 mean SST. This raises the question of how much SST feedback periodicity is necessary
397 to maintain robust eastward propagation in coupled experiments. This tendency was
398 also seen in our study, that is, slower propagation (or weaker tendency) with decreased
399 feedback frequency until the C–24days experiment (Figs. 1–7). By 1/30days, the
400 perturbations became stationary.

401 Generally, C–18days exhibited the unrealistic overestimation of intraseasonal
402 variability while maintaining eastward propagation of the MJO. Here, we are not
403 suggesting that C–18days represents the optimal SST feedback experiment. Figure 8
404 highlights the considerable differences in the simulation of MJO perturbations at phase
405 2–3 between C–18days and C–30days experiments. In C–18days, negative OLR
406 anomalies were widespread from the western IO to the MC, while in reality it should
407 be observed mainly in the IO and be accompanied by positive anomalies in the eastern
408 MC, i.e., a west-east dipolar structure (Fig. 8a). In C–30days, the OLR anomaly,
409 although was still the dominant feature in the Indian Ocean-western Pacific region,
410 became much weaker and characterized by smaller scale perturbations. These OLR
411 anomalies were generally associated with upper-level convergence (not shown)
412 embedded in much weaker wind anomalies (U200) compared to those in C–18days.
413 The circulation and OLR in C–24days exhibited the characteristics similar to those in
414 C–18days but with the OLR anomalies breaking up into smaller scales.

415 Furthermore, in the C–18days and C–24days experiments, negative anomalies
416 indicative of a downward direction in LHF and net surface heat flux (Fig. 8d, 8e, 8g,

and 8h), were predominantly observed in the convection-inactive region to the east of 150°E where low-level easterly wind and positive SST anomalies prevailed (Fig. 8j and 8k). The OLR, winds, heat fluxes, and SST to the west of 150°E exhibited similar correspondences between variables but in opposite phase. With feedback frequency reduced to 1/30days (Fig. 8f, 8i, and 8l), the heat fluxes and SST anomalies broke into unorganized smaller scaler features, consistent with the ocean temperature jump shown in Fig. 6h. Although the wind fields in the both upper and lower levels were still characterized by large-scale structure, the corresponding divergence were dominated by much smaller scale perturbations (not shown), similar to heat fluxes and SST. The increasingly dominant smaller scale perturbations can also be inferred from Fig. 2h-j and 4h-j. In addition, the large power spectra in the low frequency band spread across a wide range of wavenumbers, reflecting the smaller scale nature of the simulated perturbations in C−30days (Fig. 3j). This imparity between the scale of rotational and divergent winds suggests that the poor coupling between the convection and large-scale circulation.

With decreased feedback frequency of SST from C–CTL to C–30days, the ocean continued to receive atmospheric forcing, but the feedback response was delayed, leading to the accumulation or loss of energy (temperature) in the upper ocean, as seen in the SST distribution in the WP (Fig. 6 and 8). Subsequently, the C–30days experiment exhibited comprehensive disorder over the Indo-Pacific region, with the SST anomalies showing an unrealistically erratic spatial distribution characterized by sudden jumps (Fig. 8l) associated with plus-minus latent heat flux and 10m wind anomalies (Fig. 8f), net surface heat flux, and solar radiation (Fig. 8i). As a result, the organized large-scale circulation seen in the MJO was not manifested. To this extreme, the air−sea interaction observed in the MJO no longer worked properly in the model.

4.3 Moist static energy (MSE) budget analysis

We diagnosed the relative contribution of each term in Eq. (1) to the MSE tendency with a focus on the second (pre-conditioning) and fifth (convection crossing the MC) phases. Figure 9 illustrates the physical processes associated with each term (averaged over 10° S–0°, 120–150° E) contributing to the column-integrated MSE tendency (<dmdt>) in Eq. (1) during phase 2 in ERA5 and model simulations. In ERA5, when the MJO convection was in the eastern Indian Ocean, the column-integrated vertical and horizontal advection (-<wdmdp> and -<vdm>) over the MC area were the dominant terms in the MSE budget and largely compensated by longwave radiation and latent heat flux, as reported in Wang and Li (2020) and Tseng et al. (2022). All experiments simulated the positive and negative contributions similar to those derived from ERA5 although with different amplitudes. Notably, the C–24days and C–30days simulated relatively weak vertical advection and too strong negative latent heat flux and too weak longwave radiation flux. As a result, the C–24days and C–30days simulated relatively weak tendency compared to other experiments. The results are consistent with the poor simulation of the MJO in the extreme low frequency feedback experiments discussed above.

We compared the spatial distribution of column-integrated MSE tendency <dmdt> (shading), precipitation (contours), and 850-hPa wind (vectors) during phase 5, i.e., the period when the strongest convection crossing the MC (Fig. 10). In ERA5, the main convection (indicated by positive precipitation anomaly) is accompanied by low-level convergence in the 850-hPa wind across the MC extending into the WP (Fig. 10a). A positive <dmdt> is observed to the east of the MJO convection to the south of the equator (Fig. 10a). Conversely, a negative tendency is observed to the west of the MJO convection accompanied by negative precipitation anomalies further to the west. The phase relationship between the MSE tendency and precipitation reflects the eastward-

propagating nature of the MJO. With the exception of A–CTL, C–24days, and C–30days, the model simulations displayed a similar structure in the 20–100-day filtered <dmdt>, precipitation, and 850-hPa wind vectors (Fig. 10c–h). although the exact locations may be shifted compared to those derived from ERA5. The C–CTL simulated relatively weak signals compared to ERA5, whereas the signals became increasingly stronger with decreasing feedback frequency. The signals became unrealistically strong beyond 1/18days feedback frequency and the lead–lag relationship between the MSE tendency and precipitation became less clear. For example, positive precipitation anomaly became in phase with the tendency in the western Pacific south of the equator in C–24days and C–30days experiments, and the tendency was much weaker in C–30days. The results were consistent with the weaker eastward propagation tendency in the low-frequency feedback experiments, especially in C−24days and C−30days when the feedback frequency became unrealistically low.

The corresponding MSE budget during phase 5 is shown in Fig. 10. The MC has been identified as a barrier to the eastward propagation of the MJO (Hsu and Lee, 2005, Wu and Hsu 2009, Tseng et al. 2017, Li et al., 2020b) and approximately 30–50% of the MJO experienced stalling over the MC (Zhang and Han, 2020). To determine whether the MJO has sufficient energy to traverse the MC, we focused the analysis on phase 5. Figure 11 illustrates the projection of each MSE component and decomposition of the horizontal MSE advection at phase 5 over the MC region (20° S−20° N, 90−210° E) following the approach of Tseng et al. (2022) and Jiang et al. (2018), where F_s is total surface fluxes including SH and LH, and Q_r is vertically integrated net SW and LW radiation. Unlike in phase 2 when vertical advection is the dominant term, the MSE tendency was dominated by the horizonal MSE advection -<vdm> in ERA5 and all experiments, except the A−CTL. This contribution increased with decreasing SST feedback frequency. The weaker positive vertical advection -<wdmdp> did not vary

systematically with decreasing feedback frequency and even turned negative in C−24days and C−30days. Fs and Qr acted to damp the tendency by cancelling out the effect of the advection term. Fs tended to be more negative with decreasing feedback frequency and became much larger in C−30days. By contrast, Qr was unrealistically weak in C−18days, C−24days, and C−30days. The uncoupled simulation yielded much weaker amplitude in all terms as expected.

The -<vdm> that contributed most to the eastward propagation of the MJO in phase 5 was further decomposed into zonal (-<udmdx>) and meridional (-<vdmdy>) components to examine their relative effects (Fig. 11). Both components contributed positively, but the -<vdmdy> exhibited a larger amplitude, consistent with Tseng et al. (2014, 2022). The -<vdmdy> of high-frequency SST feedback experiments yielded results closely similar to ERA5. Comparatively, the -<vdmdy> term in low-frequency SST feedback experiments (C–18days, C–24days, and C–30days) became unrealistically large with decreasing feedback frequency and the potential jump in SST.

Spatial distributions of -<wdmdp>, -<vdm>, and 200-hPa wind at phase 5 are shown in Fig. 12. In ERA5, the wind divergence at 200 hPa at phase 5 (Fig. 12a), overlaid the 850-hPa convergence (Fig. 10a), reflecting a deep convection structure. The model simulations exhibited a similar structure to ERA5 except in A–CTL, C–24days, and C–30days experiments, and again the amplitude increased with decreasing feedback frequency. In ERA5, negative -<wdmdp> and -<vdm> anomalies (Fig. 12a) were observed to the west of the MJO convection (Fig. 10a). The spatial distribution of the negative -<vdm> anomaly (dashed-red contours) extends from the IO to the MC and positive anomaly (predominantly meridional advection from the south, not shown) in the western-central Pacific south of the equator tends to facilitate the eastward propagation of deep convection in the western Pacific, consistent with Tseng et al. (2014, 2022). The -<wdmdp> with negative and positive anomaly to the west and east

521 of the deep convection also contributes to the eastward propagation of the MJO, but
522 with weaker contribution than -<vdm>. Again, these characteristics were not simulated
523 in A–CTL, whereas the amplitudes of both terms became increasingly larger with
524 decreasing feedback frequency until becoming unrealistically large beyond 1/18days.
525 In C–30days experiment both terms exhibited unorganized spatial structure as shown
526 in preceding discussion. In summary, the high-frequency feedback experiments
527 simulated an approximately 80% projection of -<vdm> in ERA5, whereas the low-
528 frequency SST feedback experiments overestimated -<vdm> anomalies (Fig. 12f–h).
529
530 **5. Conclusions**
531 This study built upon the work of Lan et al. (2022) and Tseng et al. (2022) by
532 coupling a high-resolution 1-D TKE ocean model (the SIT model) with the CAM5, i.e.,
533 a CAM5–SIT configuration, to investigate the effects of intraseasonal SST feedback on
534 the MJO. We introduced asymmetric exchange frequencies between the atmosphere and
535 the ocean, ensuring bidirectional interaction at each timestep within the experimental
536 periodicity by fixing the SST value in the coupler. This allowed us to create SST
537 feedback with various intervals at 30 minutes, 1, 3, 6, 12, 18, 24, and 30 days.
538 The aim is to assess the effect of SST feedback frequency, namely, how often
539 should the atmosphere-driven SST change feedback to the atmosphere and whether
540 there is a limit. With the exception of the C–24days and C–30days experiment, both the
541 high-frequency and low-frequency experiments demonstrated realistic simulations of
542 various aspects of the MJO when compared to ERA5, GPCP, and OISST data, although
543 the simulation results becoming increasingly amplified and unrealistic with decreasing
544 feedback frequency. These aspects included intraseasonal periodicity (Fig. 1), eastward
545 propagation (Fig. 2 and 4), coherence in the intraseasonal band (Fig. 3), tilting vertical
546 structure (Fig. 5), intraseasonal SST (Table 2) and oceanic temperature variances (Fig.

6), the lead–lag relationship of intraseasonal variability (Fig. 7), contribution of each term to the column-integrated MSE tendency at the preconditioning phase (phase 2) and mature phased (phase 5) (Fig. 9 and Fig. 11). The MSE tendency term was dominated by the horizonal and vertical MSE advection in phase 5 and phase 2, respectively, in ERA5 and most experiments. Furthermore, we deliberately extended the SST feedback interval to an unrealistically long 30 days to investigate the limits of delayed ocean response. The main conclusion is less frequent the update, more unrealistic the simulation result.

The lead–lag relationship provides a visual representation of the variations in 20–100-day filtered LHF, FSNS, OLR, U850 and SST with positive SST anomaly leading the onset of the MJO convection (Fig. 7). This relationship highlights the interconnected nature of surface heat fluxes, solar radiation, and atmospheric circulation patterns, underscoring their mutual influence and interplay through air–sea interaction. Our results indicate that the high-frequency (low-frequency) SST experiments tended to underestimate (overestimate) the MJO simulation in CAM5–SIT model. Whether this finding can be applied to other models warrants further investigations.

The result of C–3days experiment is consistent with Stan (2018), suggesting the absence of 1–5-day variability in SST would promote the amplification of westward power associated with tropical Rossby waves. By comparing with the control experiment in which SST feedback occurs at every time step (30 minutes), the C–1day experiment (SST feedback once daily) confirmed the findings of Hagos et al. (2016) and Lan et al. (2022) that the removal of the diurnal cycle would enhance the MJO. The increasing feedback periodicity of SST in low-frequency experiments led to the accumulation of atmospheric influences through short-wave and long-wave radiations and surface heat fluxes, resulting in an unrealistically large ocean temperature

anomalies and variances within few tens of meters below ocean surface (Table 2). The large-scale nature of the MJO remains intact with decreasing feedback frequency, although becoming increasingly unrealistic in both structure and amplitude, until 1/30days when the intraseasonal fluctuations were overwhelmingly dominated by unorganized small-scale perturbations in both atmosphere and ocean, as well as at the atmosphere-ocean interface where heat and energy were rigorously exchanged.

The reason causing the sudden change between C−24days and C−30days is not entirely clear. Two possibilities are discussed here. The first possible reason leading to this disorder is that when the ocean feedback is delayed for as long as 30 days (more than half of the MJO period) both positive and negative fluxes would contribute to the heat accumulation or loss in the ocean because of the MJO phase transition and result in unorganized small scale structures in ocean temperatures, which could in turn affect the heat flux and convection. The second possible reason would be that the SST variation in a MJO event become more abrupt and may disrupt the large-scale nature of the MJO into disorganized spatial distribution in atmosphere, ocean, and the interface where rigorous heat exchange occurs. This disrupting effect of abrupt SST variation, which is not explored in this study, warrants further studies with purposedly designed expeirment to untangle.

Finally, results of intraseasonal SST feedback experiments on MJO are summarized schematically in Fig. 13, following DeMott et al. (2014). These experiments included the uncoupled experiment (A–CTL), high-frequency SST experiments (C–CTL, C–1day, and C–3days), low-frequency SST experiments (C–6days, C–12days, C–18days), and extreme low-frequency experiment (C–24days and C–30days). In the absence of intraseasonal SST variability, the eastward propagation of the MJO was disrupted, leading to weakened or fragmented MJO activity as shown in Fig. 13a. On the other hand, the high-frequency SST experiments closely mimicked

599 air–sea interaction and well captured the characteristics of the MJO. The time-varying
600 SSTs in the coupled simulation provided a certain degree of organization and sufficient
601 surface fluxes, which facilitated the development of the MJO circulation as illustrated
602 in Fig. 13b. The horizontal moist static energy tendency derived from increased low-
603 level convergence, especially due to the meridional advection of MSE, intensified the
604 MJO convection and triggered the eastward propagation over the MC region. The PBL
605 convergence ahead of the MJO convection is due to Kelvin-wave dynamics (Jiang,
606 2017), in conjunction with the background zonal flow structure (Tulich and Kiladis,
607 2021). Horizontal MSE or moisture advection in the lower troposphere, particularly the
608 seasonal mean low-level MSE influenced by the MJO's anomalous winds, has had a
609 significant impact on the MJO propagation. (Gonzalez and Jiang, 2017; Jiang, 2017).
610 This simulation result is consistent with the understanding that the MJO is primarily
611 attributed to the interaction between organized convection and large-scale circulations
612 that triggers the eastward propagation. As feedback frequency become lower, the major
613 characteristics of the MJO could still be simulated as depicted in Fig. 13c, but with
614 overestimated amplitudes and deteriorating simulations in spatial structures. In the
615 extreme low frequency experiments with frequency decreasing to 1/24days and
616 1/30days, unorganized structures started to emerge and broke up into smaller scale
617 perturbations as shown in Fig. 13d, when large-scale air–sea interaction embedded in
618 the MJO did not operate properly in the model. Eventually in the C–30days experiment,
619 unrealistically and spatially scattered anomalies in precipitation, jumping SST, surface
620 heat fluxes, and vertical and horizontal MSE advection became dominant features. All
621 these findings led to the major conclusion of this study: more spontaneous atmosphere-
622 ocean interaction (e.g., ocean response once every time step to every three days in this
623 study) with high vertical resolution in the ocean model is a key to the realistic
624 simulation of the MJO and should be properly implemented in climate models.

Code and data availability. The model code of CAM5–SIT is available at https://doi.org/10.5281/zenodo.5510795. Input data of CAM5–SIT using the climatological Hadley Centre Sea Ice and Sea Surface Temperature dataset and GODAS data forcing, including 30-year numerical experiments, are available at https://doi.org/10.5281/zenodo.5510795.

Author contributions. YYL is the CAM5–SIT model developer and writes the majority part of the paper. HHH contributes to the physical explanation and the reorganization and revision of the manuscript. WLT assists in the MSE analysis.

Competing interests. The authors declare that they have no conflict of interest.

Acknowledgements. The contribution from YYL, HHH, and WLT to this study is supported by the Ministry of Science and Technology of Taiwan under MOST 110-2123-M-001-003, MOST 110-2811-M-001-603, MOST 109-2811-M-001-624 and MOST108-2811-M-001-643. Our deepest gratitude goes to the editors and anonymous reviewers for their careful work and thoughtful suggestions that have helped improve this paper substantially. We sincerely thank the National Center for Atmospheric Research and their Atmosphere Model Working Group (AMWG) for release CESM1.2.2. We thank the computational support from National Center for High530 performance Computing of Taiwan. Thanks, ChatGPT for correcting the English grammar.

Reference

Adler, R. F., Huffman, G. J., Chang, A., Ferraro, R., Xie, P. P., Janowiak, J., Rudolf, B., Schneider, U., Curtis, S., Bolvin,

652 D., Gruber, A., Susskind, J., Arkin, P., and Nelkini, E.: The Version
653 2.1 Global Precipitation Climatology Project (GPCP) Monthly
654 Precipitation Analysis (1979 -Present), J. Hydrometeor., 4(6), 1147-
655 1167, https://doi.org/10.1175/1525-
656 7541(2003)004<1147:TVGPCP>2.0.CO;2, 2003.

657 Amante, C., and Eakins, B. W.: ETOPO1 1 arc-minute globe relief model:
658 Procedures, data sources and analysis, NOAA Tech. Memo. NESDIS
659 NGDC-24, NOAA, Silver Spring, MD, 19 pp.,
660 https://doi.org/10.7289/V5C8276M, 2009.

661 Banzon, V. F., Reynolds, R. W., Stokes, D., and Xue, Y.: A 1/4-spatial-
662 resolution daily sea surface temperature climatology based on a
663 blended satellite and in situ analysis, J. Climate, 27, 8221–8228,
664 https://doi.org/10.1175/JCLI-D-14-00293.1, 2014.

665 Behringer, D. W., and Xue, Y.: Evaluation of the global ocean data
666 assimilation system at NCEP: The Pacific Ocean. Eighth Symposium
667 on Integrated Observing and Assimilation Systems for Atmosphere,
668 Oceans, and Land Surface, AMS 84th Annual Meeting, Washington
669 State Convention and Trade Center, Seattle, Washington, 11-15.
670 Derber, J.C., and A. Rosati, 1989: A global oceanic data assimilation
671 system, J. Phys. Oceanogr., 19, 1333–1347,
672 https://ams.confex.com/ams/pdfpapers/70720.pdf, 2004.

673 Chang, M.-Y., Li, T., Lin, P.-L., and Chang, T.-H.: Forecasts of MJO
674 Events during DYNAMO with a Coupled Atmosphere-Ocean Model:
675 Sensitivity to Cumulus Parameterization Scheme, J. Meteorol.
676 Res., 33**,** 1016–1030, https://doi.org/10.1007/s13351-019-9062-5,
677 2019.

678 CLIVAR MADDEN–JULIAN OSCILLATION WORKING GROUP: MJO
679 simulation diagnostics, J. Climate, 22, 3006–3030,
680 https://doi.org/10.1175/2008JCLI2731.1, 2009.

681 DeMott, C. A., Klingaman, N. P., and Woolnough, S. J.: Atmosphere-
682 ocean coupled processes in the Madden-Julian oscillation, Rev. of
683 Geophysics, 53, 1099– 1154, https://doi.org/10.1002/2014RG00047
684 8, 2015.

685 DeMott, C. A., Stan, C., Randall, D. A., and Branson, M.
686 D.: Intraseasonal variability in coupled GCMs: The roles of ocean
687 feedbacks and model physics, J.
688 Climate, 27(13), 4970– 4995. https://doi.org/10.1175/JCLI-D-13-
689 00760.1., 2014.

690 de Szoeke, S. P., Edson, J. B., Marion, J. R., Fairall, C. W., and Bariteau,
691 L.: The MJO and air–sea interaction in TOGA COARE and
692 DYNAMO, J.
693 Climate, 28(2), 597– 622. https://doi.org/10.1175/JCLI-D-14-
694 00477.1, 2014.

695 de Szoeke, S. P., Edson, J. B., Marion, J. R., Fairall, C. W., and Bariteau,

L.: The MJO and air–sea interaction in TOGA COARE and DYNAMO, J. Climate, 28, 597–622, https://doi.org/10.1175/JCLI-D-14-00477.1, 2015.

de Szoeke, S. P., and Maloney, E.: Atmospheric mixed layer convergence from observed MJO sea surface temperature anomalies, J. Climate, 33(2), 547– 558. https://doi.org/10.1175/JCLI-D-19-0351.1, 2020.

Fu, J. X., Wang, W., Shinoda, T., Ren, H. L., and Jia, X.: Toward understanding the diverse impacts of air–sea interactions on MJO simulations, J. Geophys. Res.-Oceans,122(11), 8855– 8875. https://doi.org/10.1002/2017JC013187, 2017.

Gao, Y., Hsu, P.-C., Chen, L., Wang, L., and Li, T.: Effects of high-frequency surface wind on the intraseasonal SST associated with the Madden-Julian oscillation, Clim. Dynam., 54, 4485–4498, https://doi.org/10.1007/s00382-020-05239-w, 2020a.

Gao, Y., Klingaman, N. P., DeMott, C. A., and Hsu, P.-C.: Boreal summer intraseasonal oscillation in a superparameterized general circulation model: effects of air–sea coupling and ocean mean state, Geosci. Model Dev., 13, 5191–5209, https://doi.org/10.5194/gmd-13-5191-2020, 2020b.

Ge, X., Wang, W., Kumar, A., and Zhang, Y.: Importance of the vertical resolution in simulating SST diurnal and intraseasonal variability in an oceanic general circulation model, J. Climate, 30, 3963–3978, https://doi.org/10.1175/JCLI-D-16-0689.1, 2017.

Gonzalez, A. O., and Jiang, X.: Winter mean lower tropospheric moisture over the maritime continent as a climate model diagnostic metric for the propagation of the Madden-Julian Oscillation, Geophys. Res. Lett., 44(5), 2588–2596. https://doi.org/10.1002/2016GL072430, 2017.

Hagos, S. M., Zhang, C., Feng, Z., Burleyson, C. D., Mott, C. De, Kerns, B., Benedict, J. J., and Martini, M. N.: The impact of the diurnal cycle on the propagation of Madden-Julian Oscillation convection across the Maritime Continent, J. Adv. Model. Earth Syst., 8, 1552–1564, https://doi.org/10.1002/2016MS000725, 2016.

Hersbach, H., and Dee, D.: ERA5 reanalysis is in production, ECMWF Newsletter, Vol. 147, p. 7, https://www.ecmwf.int/en/newsletter/147/news/era5-reanalysis-production, 2016.

Hong, X., Reynolds, C. A., Doyle, J. D., May, P., and O'Neill, L.: Assessment of upper-ocean variability and the Madden-Julian Oscillation in extended-range air–ocean coupled mesoscale simulations, Dyn. Atmos. Oceans, 78, 89–105.

https://doi.org/10.1016/j.dynatmoce.2017.03.002, 2017.

Hsu, H.-H., and Lee, M.-Y.: Topographic effects on the eastward propagation and initiation of the Madden-Julian Oscillation, J. Climate, 18, 795-809, https://doi.org/10.1175/JCLI-3292.1, 2005.

Hurrell, J. W., Holland, M. M., Gent, P. R., Ghan, S., Kay, J. E., Kushner, P. J., Lamarque, J.-F., Large, W. G., Lawrence, D., Lindsay, K., Lipscomb, W. H., Long, M. C., Mahowald, N., Marsh, D. R., Neale, R. B., Rasch, P., Vavrus, S., Vertenstein, M., Bader, D., Collins, W. D., Hack, J. J., Kiehl, J., and Marshall, S.: The Community Earth System Model: A framework for collaborative research, Bull. Amer. Meteor. Soc., 94, 1339–1360, https://doi.org/10.1175/BAMS-D-12-00121.1, 2013.

Jiang, X.,Waliser, D. E., Xavier, P. K., Petch, J., Klingaman, N. P., Woolnough, S. J., Guan, B., Bellon, G., Crueger, T., DeMott, C., Hannay, C., Lin, H., Hu, W., Kim, D., Lappen, C.-L., Lu, M.-M., Ma, H.-Y., Miyakawa, T., Ridout, J. A., Schu-bert, S. D., Scinocca, J., Seo, K.-H., Shindo, E., Song, X., Stan, C., Tseng, W.-L., Wang, W., Wu, T., Wu, X., Wyser, K., Zhang, G. J., and Zhu, H.: Vertical structure and physical processes of the MaddenJulian oscillation: Exploring key model physics in climate simulations, J. Geophys. Res.-Atmos., 120, 4718–4748, https://doi.org/10.1002/2014JD022375, 2015.

Jiang, X.: Key processes for the eastward propagation of the Madden-Julian Oscillation based on multimodel simulations, J. Geophys. Res. Atmos., 122, 755–770, https://doi.org/10.1002/2016JD025955, 2017.

Jiang, X., Adames, Á. F., Zhao, M., Waliser, D., and Maloney, E.: A unified moisture mode framework for seasonality of the Madden–Julian oscillation, J. Climate, 31, 4215–4224, https://doi.org/10.1175/JCLI-D-17-0671.1, 2018.

Jiang, X., Adames, Á. F., Kim, D., Maloney, E. D., Lin, H., and Kim, H., Zhang, C., DeMott, C. A., and Klingaman, N. P.: Fifty years of research on the Madden-Julian Oscillation: Recent progress, challenges, and perspectives, J. Geophys. Res.-Atmos., 125, e2019JD030911, https://doi.org/10.1029/2019JD030911, 2020.

Kim, D., Kim, H., and Lee, M.-I.: Why does the MJO detour the Maritime continent during Austral summer? Geophys. Res. Lett., 44(5), 2579–2587, https://doi.org/10.1002/2017gl072643, 2017.

Kim, H., Vitart, F., and Waliser, D. E.: Prediction of the Madden–Julian oscillation: A review, J. Climate, 31(23), 9425– 9443, https://doi.org/10.1175/JCLI-D-18-0210.1, 2018.

Klingaman, N. P., and Demott, C. A,: Mean state biases and interannual variability affect perceived sensitivities of the Madden-Julian oscillation to air–sea coupling, J. Adv. Model. Earth Syst., 12, 1– 22, https://doi.org/10.1029/2019MS001799, 2020.

Krishnamurti, T. N., Oosterhof, D. K. and Mehta, A. V.: Air–sea interaction on the time scale of 30 to 50 days, J. Atmos. Sci., 45, 1304–1322, https://doi.org/10.1175/1520-0469(1988)045,1304:AIOTTS.2.0.CO;2, 1988.

Lambaerts, J., Lapeyre, G., Plougonven, R., and Klein, P.: Atmospheric response to sea surface temperature mesoscale structures, J. Geophys. Res.-Atmos., 118(17), 9611–9621. https://doi.org/10.1002/jgrd.50769, 2020.

Lan, Y.-Y., Hsu, H.-H., Tseng, W.-L., and Jiang, L.-C.: Embedding a one-column ocean model in the Community Atmosphere Model 5.3 to improve Madden–Julian Oscillation simulation in boreal winter, Geosci. Model Dev., 15, 5689–5712, https://doi.org/10.5194/gmd-15-5689-2022, 2022.

Li, Y., Han, W., Shinoda, T., Wang, C., Ravichandran, M., and Wang, J.-W.: Revisiting the wintertime intraseasonal SST variability in the tropical south Indian Ocean: Impact of the ocean interannual variation, J. Phys. Oceanogr., 44, 1886–1907, https://doi.org/10.1175/JPO-D-13-0238.1, 2014.

Li, T., Ling, J., and Hsu, P.-C.: Madden–Julian Oscillation: Its discovery, dynamics, and impact on East Asia, J. Meteor. Res., 34, 20–42, https://doi.org/10.1007/s13351-020-9153-3, 2020a.

Li, K., Yu, W., Yang, Y., Feng, L., Liu, S., and Li, L.: Spring barrier to the MJO eastward propagation, Geophys. Res. Lett., 47, e2020GL087788, https://doi.org/10.1029/2020GL087788, 2020b.

Liang, Y.; Du, Y.; Zhang, L.; Zheng, X.; Qiu, S. The 30–50-Day Intraseasonal Oscillation of SST and Precipitation in the South Tropical Indian Ocean, Atmos., 9, 69. https://doi.org/10.3390/atmos9020069, 2018.

Liang, Y., and Du, Y.: Oceanic impacts on 50–80-day intraseasonal oscillation in the eastern tropical Indian Ocean, Clim. Dynam., 59, 1283–1296, https://doi.org/10.1007/s00382-021-06041-y, 2022.

Liebmann, B.: Description of a complete (interpolated) outgoing longwave radiation dataset, B. Am. Meteorol. Soc., 77, 1275–1277, 1996.

Madden, R. A., and Julian, P. R.: Description of global-scale circulation cells in the tropics with a 40-50 day period, J. Atmos. Sci., 29, 1109-1123, https://doi.org/10.1175/1520-0469(1972)029<1109:DOGSCC>2.0.CO;2, 1972.

Maloney, E., and Sobel, A. H.: Surface fluxes and ocean coupling in the tropical intraseasonal oscillation. J. Climate, 17, 4368–4386, https://doi.org/10.1175/JCLI-3212.1, 2004.

Newman, M., Sardeshmukh, P. D., and Penland, C.: How important is

air–sea coupling in ENSO and MJO evolution? J. Climate, 22, 2958– 2977, https://doi.org/10.1175/2008JCLI2659.1, 2009.

Pariyar, S.K., Keenlyside, N., Tseng, W.-L., Hsu, H.-H., and Tsuang, B.-J. The role of air–sea coupling on November–April intraseasonal rainfall variability over the South Pacific, Clim. Dynam., 60, 1121–1136, https://doi.org/10.1007/s00382-022-06354-6, 2023.

Pei, S., Shinoda, T., Soloviev, A., and Lien, R.-C.: Upper ocean response to the atmospheric cold pools associated with the Madden-Julian Oscillation, Geophys. Res. Lett., 45, 5020–5029, https://doi.org/10.1029/2018GL077825, 2018.

Rasch, P. J., Xie, S., Ma, P.-L., Lin, W., Wang, H., Tang, Q., Bur- rows, S. M., Caldwell, P., Zhang, K., Easter, R. C., Cameron- Smith, P., Singh, B., Wan, H., Golaz, J.-C., Harrop, B. E., Roesler, E., Bacmeister, J., Larson, V. E., Evans, K. J., Qian, Y., Taylor, M., Leung, L. R., Zhang, Y., Brent, L., Branstet- ter, M., Hannay, C., Mahajan, S., Mametjanov, A., Neale, R., Richter, J. H., Yoon, J.-H., Zender, C. S., Bader, D., Flan- ner, M., Foucar, J. G., Jacob, R., Keen, N., Klein, S. A., Liu, X., Salinger, A. G., Shrivastava, M., and Yang, Y.: An overview of the atmospheric component of the Energy Exascale Earth System Model, J. Adv. Model Earth Sy., 11, 2377–2411, https://doi.org/10.1029/2019ms001629, 2019.

Rayner, N. A., Parker, D. E., Horton, E. B., Folland, C. K., Alexander, L. V., Rowell, D. P., Kent, E. C., and Kaplan, A.: Global analyses of sea surface temperature, sea ice, and night marine air temperature since the late nineteenth century, J. Geophys. Res., 108(D14), 4407, https://doi.org/10.1029/2002JD002670, 2003.

Ren, P. F., Gao, L., Ren, H.-L., Rong, X., and Li, J.: Representation of the Madden–Julian Oscillation in CAMSCSM, J. Meteor. Res., 33, 627–650, https://doi.org/10.1007/s13351-019-8118-x, 2019.

Savarin, A., and Chen, S. S.: Pathways to better prediction of the MJO: 2. Impacts of atmosphere-ocean coupling on the upper ocean and MJO propagation, J. Adv. Model. Earth Syst., 14, e2021MS002929, https://doi.org/10.1029/2021MS002929, 2022.

Shinoda, T., Pei, S., Wang, W., Fu, J. X., Lien, R.-C., Seo, H., and Soloviev, A.: Climate process team: Improvement of ocean component of NOAA climate forecast system relevant to Madden-Julian Oscillation simulations, J. Adv. Model. Earth Syst., 13(12), e2021MS002658. https://doi.org/10.1029/2021MS002658, 2021.

Seo, H., Subramanian, A. C., Miller, A. J., and Cavanaugh, N. R.: Coupled impacts of the diurnal cycle of sea surface temperature on the Madden–Julian oscillation, J. Climate, 27(22), 8422– 8443. https://doi.org/10.1175/JCLI-D-14-00141.1, 2014.

871 Sobel, A. H., and Gildor, H.: A simple time-dependent model of SST hot
872 spots. J. Climate, 16, 3978–3992, https://doi.org/10.1175/1520-
873 0442(2003)016<3978:ASTMOS>2.0.CO;2, 2003.

874 Sobel, A. H., Maloney, E. D., Bellon, G., and Frierson, D. M.: Surface
875 Fluxes and Tropical Intraseasonal Variability: a Reassessment, J.
876 Adv. Model. Earth Syst., 2, 2,
877 https://doi.org/10.3894/JAMES.2010.2.2, 2010.

878 Sobel, A., Wang, S., and Kim, D.: Moist static energy budget of the MJO
879 during DYNAMO, J. Atmos. Sci., 71(11), 4276– 4291,
880 https://doi.org/10.1175/JAS-D-14-0052.1, 2014.

881 Stan, C.: The role of SST variability in the simulation of the MJO, Clim.
882 Dynam., 51, 2943–2964, https://doi.org/10.1007/s00382-017-4058-
883 2, 2018.

884 Tseng, W.-L., Tsuang, B.-J., Keenlyside, N. S., Hsu, H.-H. and Tu, C.-
885 Y.: Resolving the upper-ocean warm layer improves the simulation
886 of the Madden-Julian oscillation, Clim. Dynam., 44, 1487–1503,
887 https://doi.org/10.1007/s00382-014-2315-1, 2015.

888 Tseng, W.-L., Hsu, H.-H., Keenlyside, N., Chang, C.-W. J., Tsuang, B.-
889 J., Tu, C.-Y., and Jiang, L.-C.: Effects of Orography and Land–Sea
890 Contrast on the Madden–Julian Oscillation in the Maritime
891 Continent: A Numerical Study Using ECHAM-SIT, J. Climate, 30,
892 9725–9741, https://doi.org/10.1175/JCLI-D-17-0051.1, 2017.

893 Tseng, W.-L., Hsu, H.-H., Lan, Y.-Y., Lee, W.-L., Tu, C.-Y., Kuo, P.-
894 H., Tsuang, B.-J., and Liang, H.-C.: Improving Madden–Julian
895 oscillation simulation in atmospheric general circulation models by
896 coupling with a one-dimensional snow–ice–thermocline ocean
897 model, Geosci. Model Dev., 15, 5529–5546,
898 https://doi.org/10.5194/gmd-15-5529-2022, 2022.

899 Tulich, S. N., and Kiladis, G. N.: On the Regionality of moist kelvin
900 waves and the MJO: The critical role of the background zonal flow,
901 J. Adv. Model. Earth Syst., 13(9), e2021MS002528.
902 https://doi.org/10.1029/2021MS002528, 2021.

903 Voldoire, A., Roehrig, R., Giordani, H., Waldman, R., Zhang, Y., Xie,
904 S., and Bouin, M.-N.: Assessment of the sea surface temperature
905 diurnal cycle in CNRM-CM6-1 based on its 1D coupled
906 configuration, Geosci. Model Dev., 15, 3347–3370,
907 https://doi.org/10.5194/gmd-15-3347-2022, 2022.

908 Wang, W., Hung, M.-P., Weaver, S. J., Kumar, A., and Fu, X.: MJO
909 prediction in the NCEP Climate Forecast System version 2, Clim.
910 Dynam., 42, 2509–2520, https://doi.org/10.1007/s00382-013-1806-
911 9, 2014.

912 Wang, L. and Li, T.: Effect of vertical moist static energy advection on
913 MJO eastward propagation: Sensitivity to analysis domain, Clim.
914 Dynam., 54, 2029–2039, https://doi.org/10.1007/s00382-019-

915 05101-8, 2020.

916 Watterson, I. G.: The sensitivity of subannual and intraseasonal tropical
917 variability to model ocean mixed layer depth, J. Geophys. Res., 107,
918 4020, https://doi.org/10.1029/2001JD000671, 2002.

919 Wheeler, M. C., and Hendon, H. H.: An all-season real-time multivariate
920 MJO index: development of an index for monitoring and prediction,
921 Mon. Weather Rev., 132, 1917–1932, https://doi.org/10.1175/1520-
922 0493(2004)132<1917:AARMMI>2.0.CO;2, 2004.

923 Wheeler, M., and Kiladis, G. N.: Convectively coupled equatorial waves:
924 Analysis of clouds and temperature in the wavenumber-frequency
925 domain, J. Atmos. Sci., 56, 374– 399, https://doi.org/10.1175/1520-
926 0469(1999)056<0374:CCEWAO>2.0.CO;2, 1999.

927 Wu, C.-H., and Hsu, H.-H.: Potential Influence of Topography on the
928 MJO in the Maritime Continent, J. Climate, 22, 5433-5448,
929 https://doi.org/10.1175/2009JCLI2825.1, 1999.

930 Wu, J., Li, Y., Luo, J.-J. and Jiang, X.: Assessing the role of air–sea
931 coupling in predicting Madden–Julian oscillation with an
932 Atmosphere–Ocean coupled model, J. Clim. 34 9647–63,
933 https://doi.org/10.1175/JCLI-D-20-0989.1, 2021.

934 Zhang, L., and Han, W.: Barrier for the eastward propagation of
935 Madden–Julian Oscillation over the maritime continent: A possible
936 new mechanism, Geophys. Res. Lett., 47(21),
937 e2020GL090211. https://doi.org/10.1029/2020gl090211, 2020.

938 Zhao, N., and Nasuno, T.: How Does the Air–Sea Coupling Frequency
939 Affect Convection During the MJO Passage?, J. Adv. Model. Earth
940 Sy., 12, e2020MS002058, https://doi.org/10.1029/2020MS002058,
941 2020.

Table 1. Two sets of experiments with different SST feedback frequencies: high-frequency (C–CTL, C–1day and C–3days) and low-frequency (C–6days, C–12days, C–18days, C–24days and C–30days).

subseasonal sets	**high-frequency SST (< 6 days)**			**low-frequency SST (6-30 days)**				
experiments	C–CTL	C–1day	C–3days	C–6days	C–12days	C–18days	C–24days	C–30days
atmosphere to ocean frequency	48/1day							
ocean to atmosphere Frequency	48/1day	1/1day	1/3days	1/6days	1/12days	1/18days	1/24days	1/30days

Table 2. Key intraseasonal (20–100-day bandpass filtered) ocean temperatures in all experiments: SST, differences between SST and temperatures at 10m depth ($\overline{\Delta T}_{0-10m}$) and 30m depth ($\overline{\Delta T}_{0-30m}$), t max/mini SST and 10m-depth temperature (T_{10m}) in the area of (110–130° E, 5–15° S) during a MJO cycle for the observation (OISST), AGCM (A–CTL), high-frequency experiments (C–CTL, C–1day, and C–3days), and low-frequency experiments (C–6days, C–12days, C–18days, C–24days, and C–30days)

(110–130° E, 5–15° S)		obs.	AGCM	high-frequency			low-frequency				
experiments		OISST[1]	A–CTL[2]	C–CTL	C–1day	C–3days	C–6days	C–12days	C–18days	C–24days	C–30days
DJF seasonal mean	SST	302.2 ±0.96	302.2 ±0.77	300.8 ±0.76	301.2 ±0.76	301.2 ±0.75	301.2 ±0.75	301.4 ±0.75	301.6 ±0.80	302.0 ±1.06	302.7 ±1.71
	$\overline{\Delta T}_{0-10m}$	-	-	0.1 ± 0.22	0.1 ± 0.22	0.1 ± 0.21	0.1 ± 0.23	0.2 ± 0.25	0.3 ± 0.32	0.5 ± 0.50	1.0 ± 0.95
	$\overline{\Delta T}_{0-30m}$	-	-	0.8 ± 0.79	0.7 ± 0.70	0.6 ± 0.69	0.8 ± 0.70	0.8 ± 0.70	1.0 ± 0.73	1.4 ± 0.96	2.1 ± 1.54
phase's mean in boreal winter	max SST (phase)	0.21 (ph2)	0.02 (ph2)	0.24 (ph3)	0.26 (ph3)	0.22 (ph3)	0.32 (ph3)	0.36 (ph3)	0.43 (ph3)	0.50 (ph3)	0.62 (ph2)
	max T_{10m} (phase)	-	-	0.15 (ph4)	0.17 (ph4)	0.14 (ph3)	0.19 (ph3)	0.21 (ph3)	0.26 (ph3)	0.30 (ph3)	0.35 (ph2)
	mini SST (phase)	-0.21 (ph7)	-0.003 (ph8)	-0.17 (ph7)	-0.22 (ph7)	-0.19 (ph7)	-0.25 (ph7)	-0.28 (ph7)	-0.38 (ph7)	-0.52 (ph6)	-0.60 (ph6)
	mini T_{10m} (phase)	-	-	-0.11 (ph8)	-0.12 (ph7)	-0.11 (ph8)	-0.15 (ph7)	-0.17 (ph7)	-0.24 (ph7)	-0.33 (ph6)	-0.33 (ph6)

Note: [1]daily average data, [2] monthly average data.

Figure List

Figure 1. Wavenumber–frequency spectra for 850-hPa zonal wind averaged over 10° S–10° N in boreal winter after removing the climatological mean seasonal cycle. Vertical dashed lines represent periods at 80 and 30 days. (a)–(j) are from ERA5 reanalysis, A–CTL, C–CTL, C–1day, C–3days, C–6days, C–12days, C–18days, C–24days, and C–30days, respectively.

Figure 2. Hovmöller diagrams of correlation between precipitation averaged over 10° S–5° N, 75–100° E and precipitation (color) and 850-hPa zonal wind (contour) averaged over 10° N–10° S. (a)–(j) are arranged in the same order as in Fig. 1 for GPCP/ERA5 and all experiments. All data are 20–100-day bandpass filtered.

Figure 3. Zonal wavenumber–frequency power spectra of anomalous OLR (colors) and phase lag with U850 (vectors) for the symmetric component of tropical waves, with the vertically upward vector representing a phase lag of 0° and phase lag increasing clockwise. Three dispersion straight lines with increasing slopes representing the equatorial Kelvin waves (derived from the shallow water equations) corresponding to three equivalent depths, 12, 25, and 50 m, respectively. (a)–(j) are arranged in the same order as in Fig. 1 for NOAA/ERA5 and all experiments.

Figure 4. Phase-longitude Hovmöller diagrams of 20–100-day filtered precipitation (mm day^{-1}, shaded) and SST anomaly (K, contour) averaged over 10° N–10° S from phase 1 to 8. Contour interval is 0.03; solid, dashed, and thick-black lines represent positive, negative, and zero values, respectively. (a)–(j) are arranged in the same order as in Fig. 1 for NOAA/ERA5 and all experiments.

Figure 5. Phase-vertical Hovmöller diagrams of 20–100-day specific humidity (shading, g kg^{-1}) and air temperature (contoured, K) averaged over 5–20° S, 120–150° E; solid, dashed, and thick-black curves are positive, negative, and zero values, respectively. (a)–(j) are arranged in the same order as in Fig. 1 for NOAA/ERA5 and all experiments.

Figure 6. The 20–100-day filtered oceanic temperature (K, shaded and contour, interval 0.03) at phase 2–3 (Left column) and phase 4–5 (Right column) averaged over 0–15° S between 0 and 60 m depth. (a)–(b) are from C–CTL, (c)–(d) are from C–1day, (e)–(f) are from C–3days, (g)–(h) are from C–6days, (i)–(j) are from C–12days, (k)–(l) are from C–18days, (m)–(n) are from C–24days, and (o)–(p) are from C–30days.

Figure 7. The lead–lag relationship between MJO-related atmosphere and SST variation from phase 1 to 8 averaged within 110–130° E and 5–15° S. The variables analyzed include 20-100-day filtered LHF, green shading), OLR (yellow bar chart), FSNS, (orange bar chart), U850 (purple bar chart), 30-m T (multiplied by 100, black line), and SST (multiplied by 10, orange line). Variables denoted with L (R) are scaled by the left (right) y-axis. (a)–(j) are from ERA5/OISST reanalysis, A–CTL, C–CTL, C–1day, C–3days, C–6days, C–12days, C–18days, C–24days, and C–30days, respectively.

Figure 8. Averaged 20–100-day filtered fields at phase 2–3. (Upper row) OLR (W m^{-2}, shaded) and 200 hPa zonal and meridional wind anomaly (m s^{-1}, vector with reference vector shown at the top right corner, latent heat flux (W m^{-2}, shaded, positive representing upward), and 10-m wind anomaly (m s^{-1}, contour interval 0.5). (Second row) net surface heat flux (W m^{-2}, shaded) and net solar radiation (W m^{-2}, contour interval 6). (Third row) SST (K, shaded) and 850 hPa zonal and meridional wind anomaly (m s^{-1}, vector with reference vector shown at the top right corner. The number of days used to generate the composite is shown at the bottom right corner. (a), (d), (g) and (j) are from C–18days; (b), (e), (h) and (k) are from C–24days, and (c), (f), (i) and (l) are from C–30days, respectively. Solid, dashed, and thick-black lines represent positive, negative, and zero values, respectively.

Figure 9. Averaged 20–100-day filtered column-integrated MSE budget terms (J kg^{-1} s^{-1}) in 10° S–0° N/S, 120–150° E for ERA5 and all model simulations. Colors represent different datasets: green for REA5, light blue for A–CTL, red, orange and navy blue for high-frequency experiments (C–CTL, C–1day, and C–3days, respectively), purple, black, dark brown, dark green, and dark gray for low-frequency experiments (C–6days, C–12days, C–18days, C–24days, and C–30days, respectively). The bars from left to right represent MSE tendency (<dmdt>), vertical MSE advection (-<wdmdp>), horizontal MSE advection (-<vdm>), surface latent heat flux (LH), surface sensible heat flux (SH), shortwave radiation flux (<SW>), longwave radiation flux (<LW>), and residual terms.

Figure 10. Filtered the column-integrated MSE tendency (J kg^{-1} s^{-1}, shading), precipitation (mm d^{-1}, contours interval 1.5) and 850-hPa wind (green vector, reference vector 2 m s^{-1}) in phase 5: (a) ERA5, (b) A−CTL, (c) C−CTL, (d) C−1day, (e) C−3days, (f) C−6days, (g) C−12days, (h) C−18days, (i) C−24days, and (i) C−30days. Solid-red, dashed-blue, and thick-black curves represent positive, negative, and zero values, respectively.

Figure 11. The projection of each MSE component onto the ERA5 column-integrated MSE tendency at phase 5 over the MC (20° S–20° N, 90–210° E): <dmdt>, -<wdmdp>, -<vdm>, Qr, Fs, and residual; decomposition of horizontal MSE advection to zonal and meridional advection (-<udmdt> and -<vdmdy>).

Figure 12. Filtered column-integrated vertical (J kg^{-1} s^{-1}, shading) and horizontal MSE advection (J kg^{-1} s^{-1}, contours interval 6.0), and 200-hPa wind (green vector with reference vector 3 m s^{-1}): (a) ERA5, (b) A−CTL, (c) C−CTL, (d) C−1day, (e) C−3days, (f) C−6days, (g) C−12days, (h) C−18days, (i) C−24days, and (j) C−30days. Solid-blue, dashed-red, and thick-black curves represent positive, negative, and zero values, respectively.

Figure 13. Schematic diagrams illustrate the anomalous circulation and moistening processes during the eastward propagation of the MJO in experiments: (a) A−CTL, (b) high-frequency SST feedback experiments (C−CTL, C−1day, and C−3days), (c) low-frequency SST feedback experiments (C−6days, C−12days, and C−18days), and (d) C−24days and C−30days experiment. In each panel, the horizontal line represents the equator. The size of clustering gray clouds indicates the strength of convective organization. A red ellipse indicates convection-driven circulation. In the coupled simulations, light red (blue) filled ovals represent warm (cold) SST anomalies, respectively, and grass green filled rectangle represent latent heat flux. Unresolved convective processes are indicated by black dots representing low-level moisture convergence. Low-level moisture convergence into the equatorial trough is shown by light blue arrows, while midlevel moisture advection is represented by left-pointing green arrows. The deeper colors or thicker lines on the map indicate stronger anomalies of the MJO perturbations. Note: The concept of the figure is based on DeMott et al. (2014).

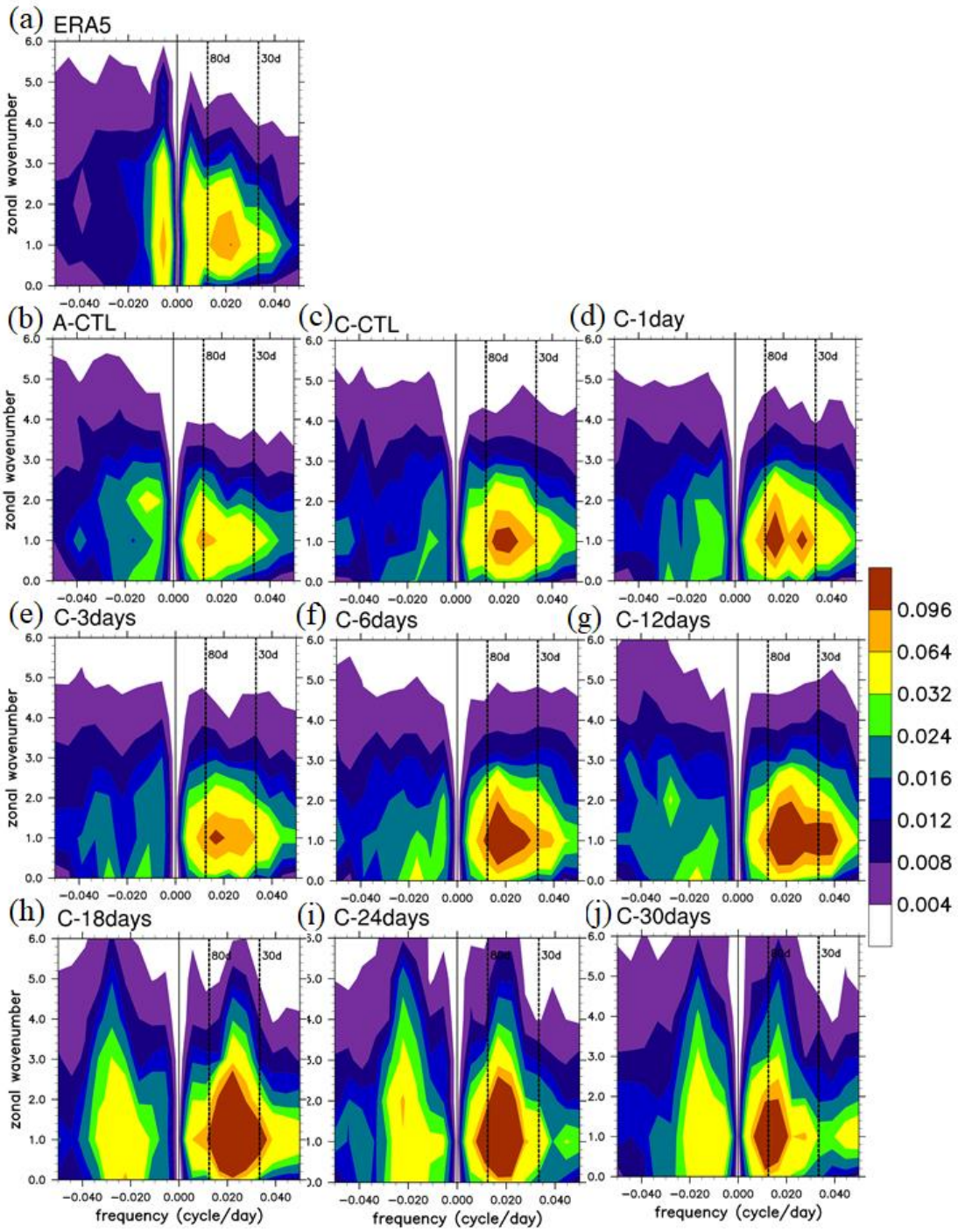

Figure 1. Wavenumber–frequency spectra for 850-hPa zonal wind averaged over 10° S–10° N in boreal winter after removing the climatological mean seasonal cycle. Vertical dashed lines represent periods at 80 and 30 days. (a)–(j) are from ERA5 reanalysis, A–CTL, C–CTL, C–1day, C–3days, C–6days, C–12days, C–18days, C–24days, and C–30days, respectively.

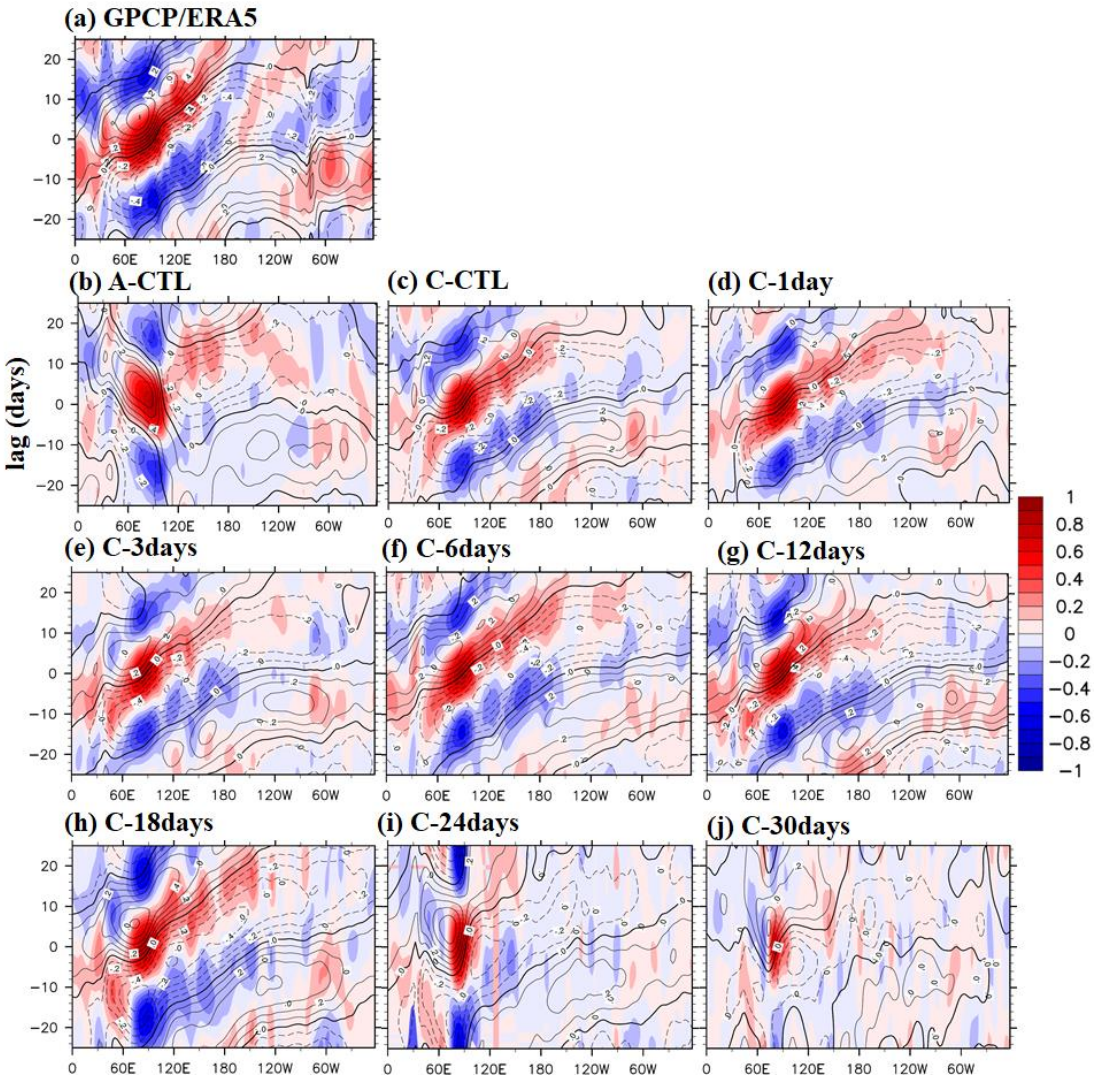

Figure 2. Hovmöller diagrams of correlation between precipitation averaged over 10° S–5° N, 75–100° E and precipitation (color) and 850-hPa zonal wind (contour) averaged over 10° N–10° S. (a)–(j) are arranged in the same order as in Fig. 1 for GPCP/ERA5 and all experiments. All data are 20–100-day bandpass filtered.

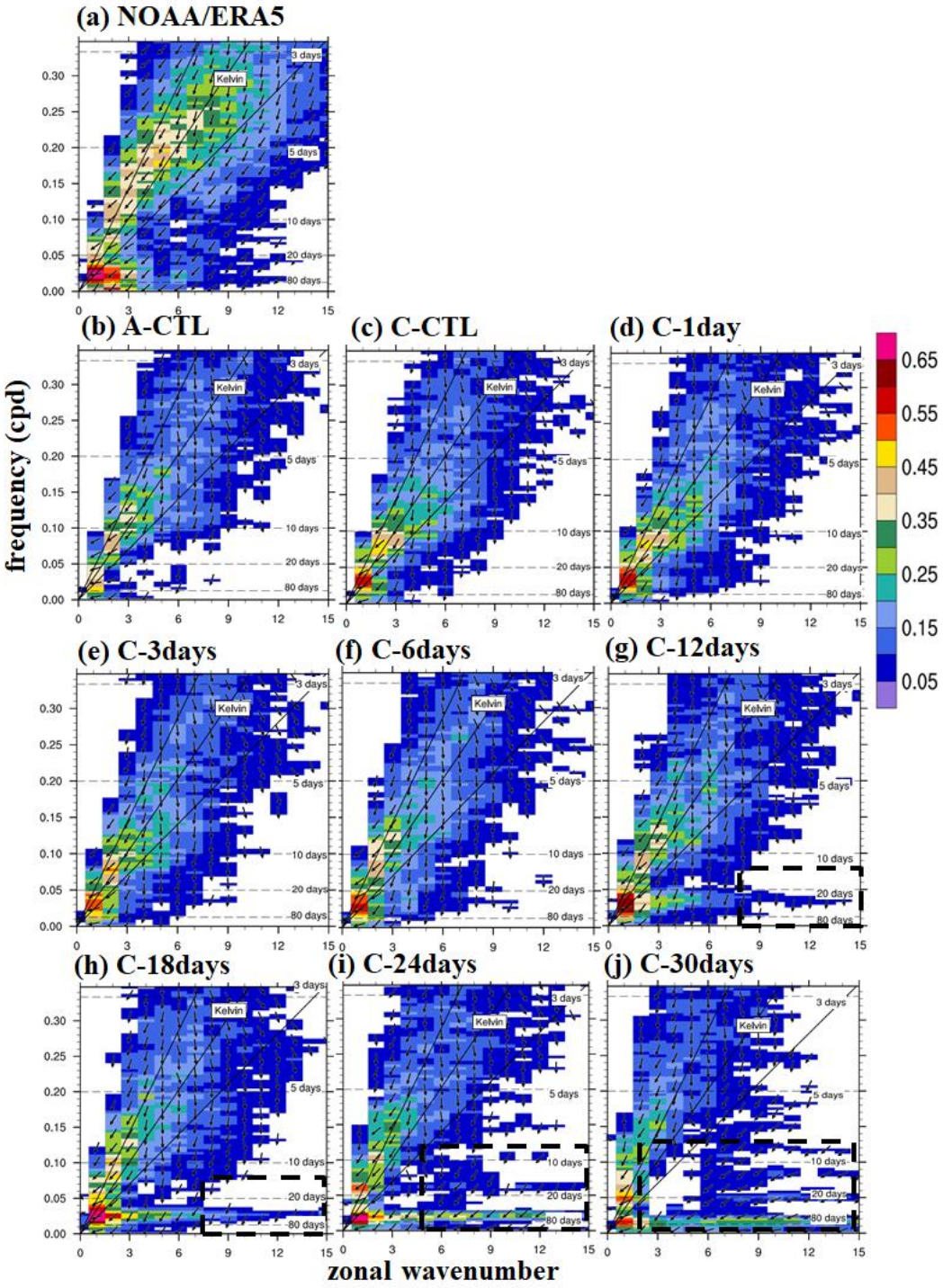

Figure 3. Zonal wavenumber–frequency power spectra of anomalous OLR (colors) and phase lag with U850 (vectors) for the symmetric component of tropical waves, with the vertically upward vector representing a phase lag of 0° with phase lag increasing clockwise. Three dispersion straight lines with increasing slopes represent the equatorial Kelvin waves (derived from the shallow water equations) corresponding to three equivalent depths, 12, 25, and 50 m, respectively. (a)–(j) arrange in order are same order as in Fig. 1 for NOAA/ERA5 and all experiments.

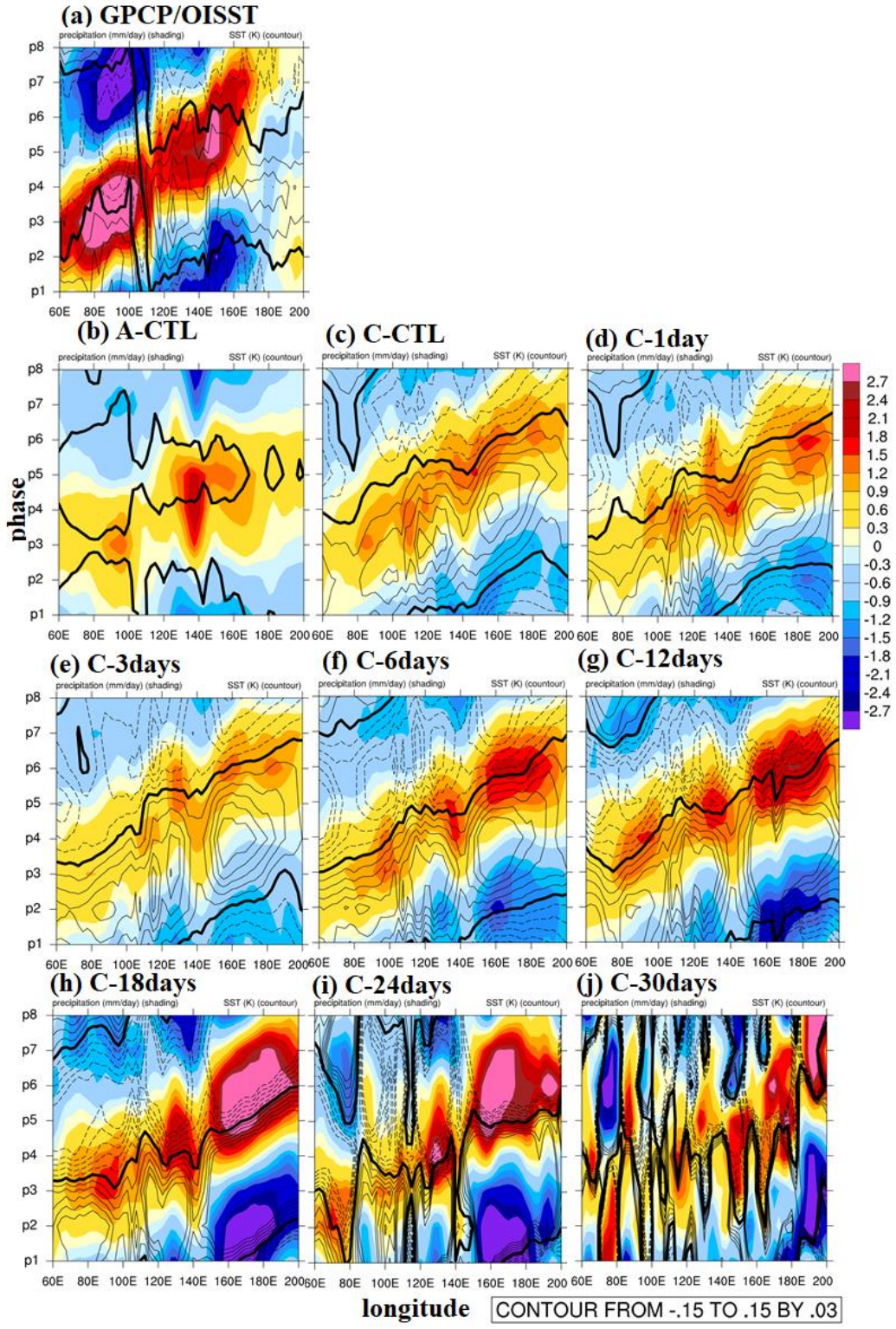

Figure 4. Phase-longitude Hovmöller diagrams of 20–100-day filtered precipitation (mm day^{-1}, shaded) and SST anomaly (K, contour) averaged over 10° N–10° S from phase 1 to 8. Contour interval is 0.03; solid, dashed, and thick-black lines represent positive, negative, and zero values, respectively. (a)–(j) are arranged in the same order as in Fig. 1 for NOAA/ERA5 and all experiments.

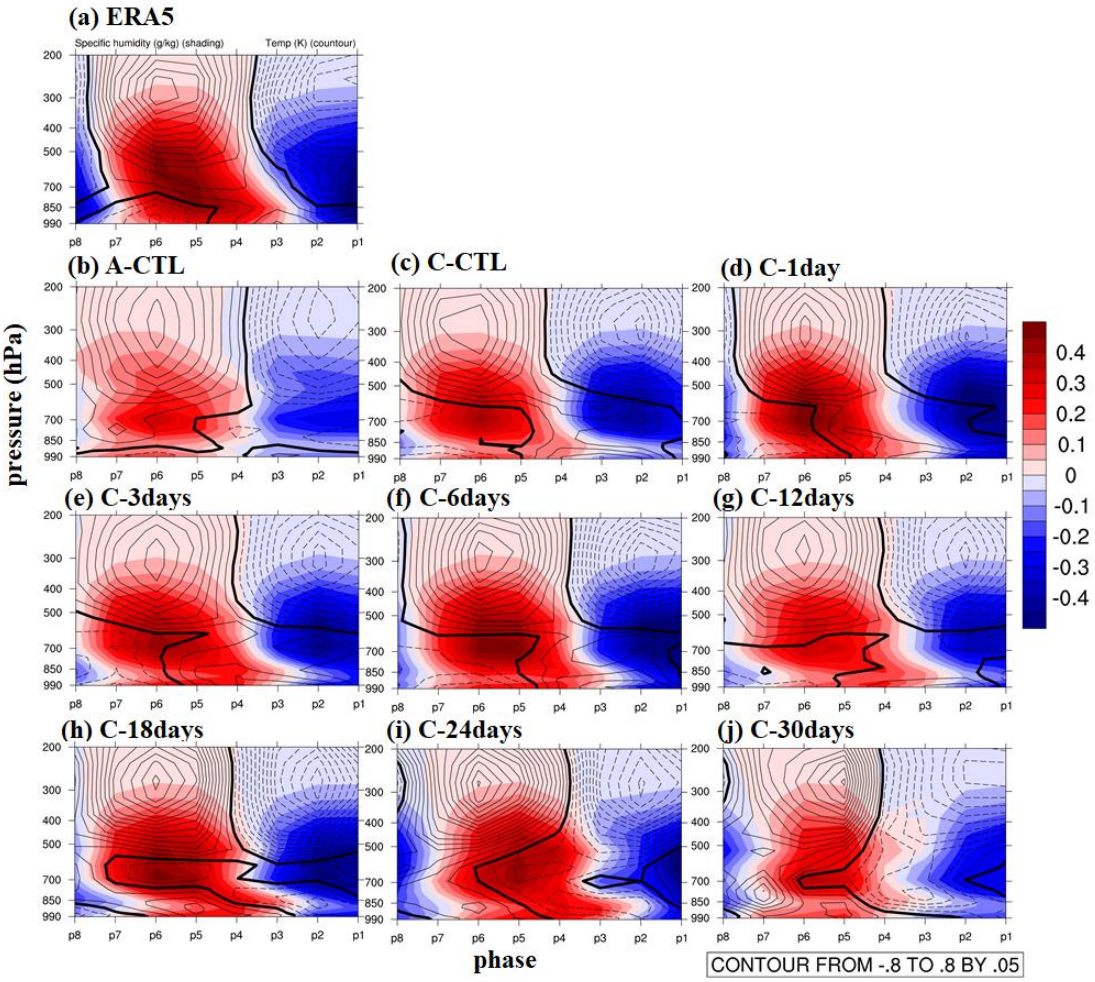

Figure 5. Phase-vertical Hovmöller diagrams of 20–100-day specific humidity (shading, g kg−1) and air temperature (contoured, K) averaged over 5–20° S, 120–150° E; solid, dashed, and thick-black curves are positive, negative, and zero values, respectively. (a)–(j) are arranged in the same order as in Fig. 1 for NOAA/ERA5 and all experiments.

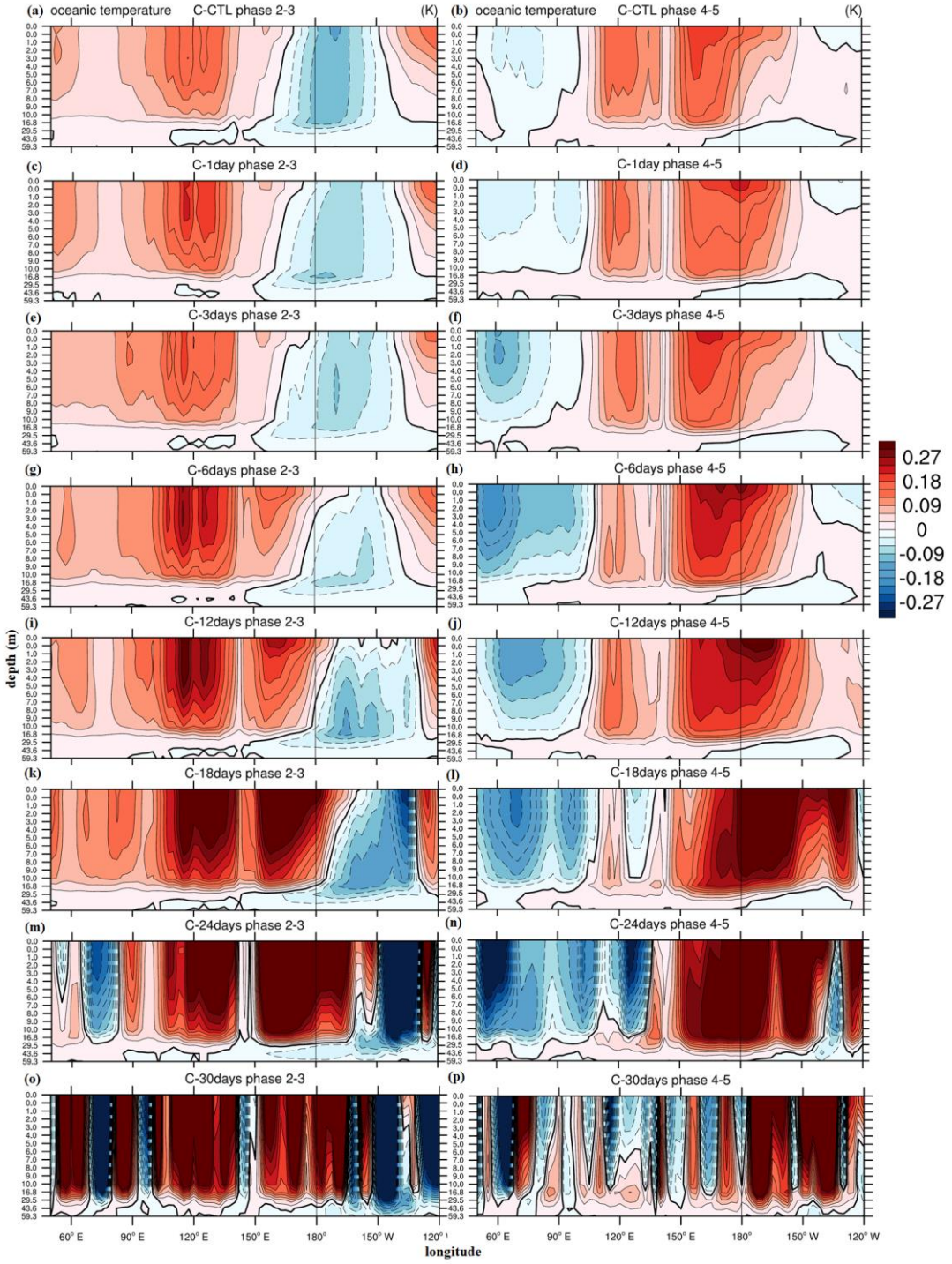

Figure 6. The 20–100-day filtered oceanic temperature (K, shaded and contour, interval 0.03) at phase 2–3 (Left column) and phase 4–5 (Right column) averaged over 0–15° S between 0 and 60 m depth. (a)–(b) are from C–CTL, (c)–(d) are from C–1day, (e)–(f) are from C–3days, (g)–(h) are from C–6days, (i)–(j) are from C–12days, (k)–(l) are from C–18days, (m)–(n) are from C–24days, and (o)–(p) are from C–30days.

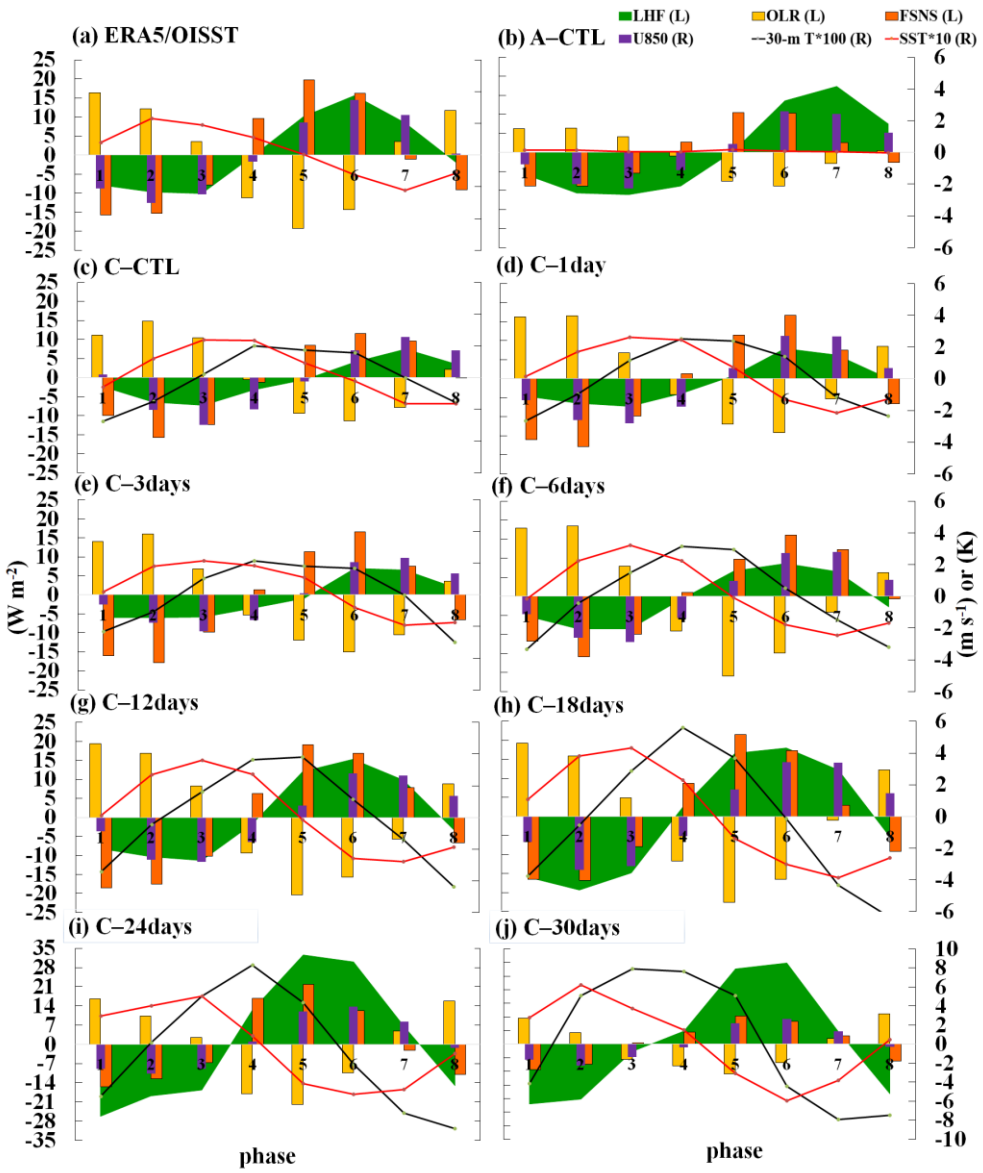

Figure 7. The lead–lag relationship between MJO-related atmosphere and SST variation from phase 1 to 8 averaged within 110–130° E and 5–15° S. The variables analyzed include 20-100-day filtered LHF, green shading), OLR (yellow bar chart), FSNS, (orange bar chart), U850 (purple bar chart), 30-m T (multiplied by 100, black line), and SST (multiplied by 10, orange line). Variables denoted with L (R) are scaled by the left (right) y-axis. (a)–(j) are from ERA5/OISST reanalysis, A–CTL, C–CTL, C–1day, C–3days, C–6days, C–12days, C–18days, C–24days, and C–30days, respectively.

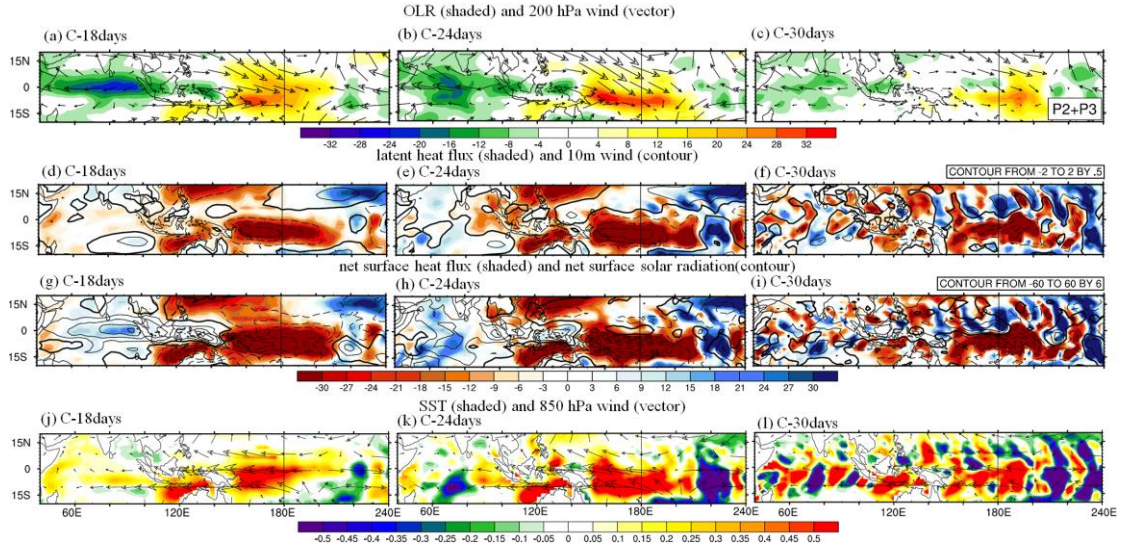

Figure 8. Averaged 20–100-day filtered fields at phase 2–3. (Upper row) OLR (W m^{-2}, shaded) and 200 hPa zonal and meridional wind anomaly (m s^{-1}, vector with reference vector shown at the top right corner, latent heat flux (W m^{-2}, shaded, positive representing upward), and 10-m wind anomaly (m s^{-1}, contour interval 0.5). (Second row) net surface heat flux (W m^{-2}, shaded) and net solar radiation (W m^{-2}, contour interval 6). (Third row) SST (K, shaded) and 850 hPa zonal and meridional wind anomaly (m s^{-1}, vector with reference vector shown at the top right corner. The number of days used to generate the composite is shown at the bottom right corner. (a), (d), (g) and (j) are from C–18days; (b), (e), (h) and (k) are from C–24days, and (c), (f), (i) and (l) are from C–30days, respectively. Solid, dashed, and thick-black lines represent positive, negative, and zero values, respectively.

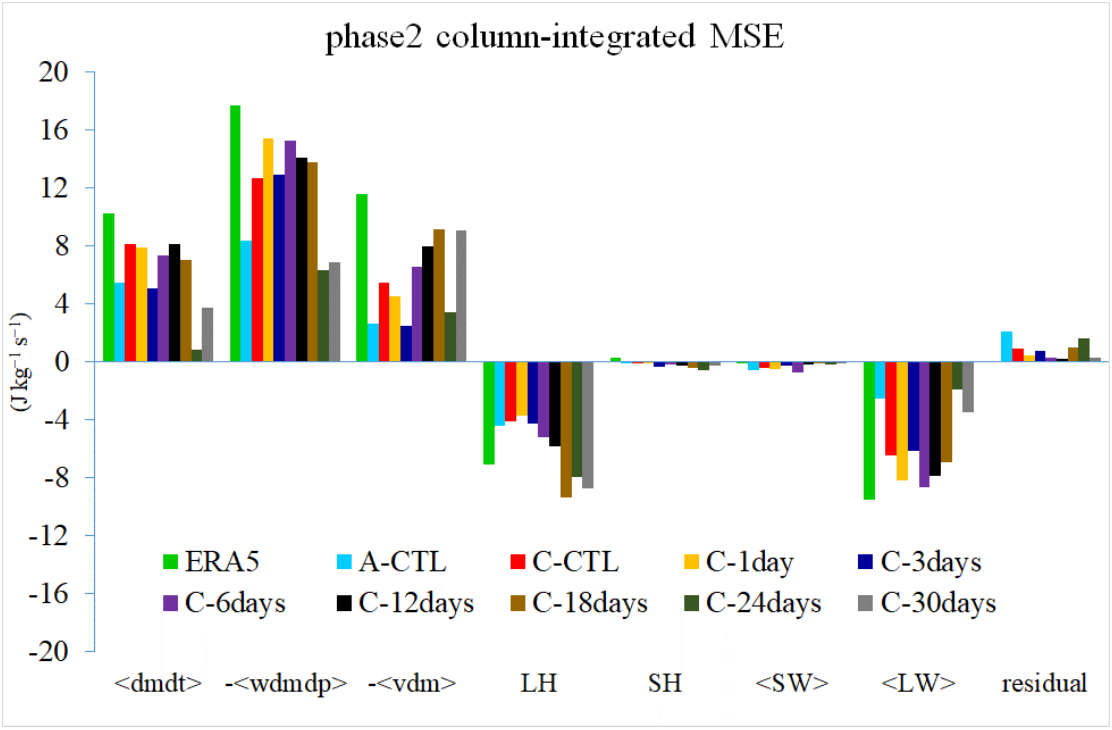

Figure 9. Averaged 20–100-day filtered column-integrated MSE budget terms (J kg−1 s−1) in 10° S–0° N/S, 120–150° E for ERA5 and all model simulations. Colors represent different datasets: green for REA5, light blue for A–CTL, red, orange and navy blue for high-frequency experiments (C–CTL, C–1day, and C–3days, respectively), purple, black, dark brown, dark green, and dark gray for low-frequency experiments (C–6days, C–12days, C–18days, C–24days, and C–30days, respectively). The bars from left to right represent MSE tendency (<dmdt>), vertical MSE advection (-<wdmdp>), horizontal MSE advection (-<vdm>), surface latent heat flux (LH), surface sensible heat flux (SH), shortwave radiation flux (<SW>), longwave radiation flux (<LW>), and residual terms.

1133

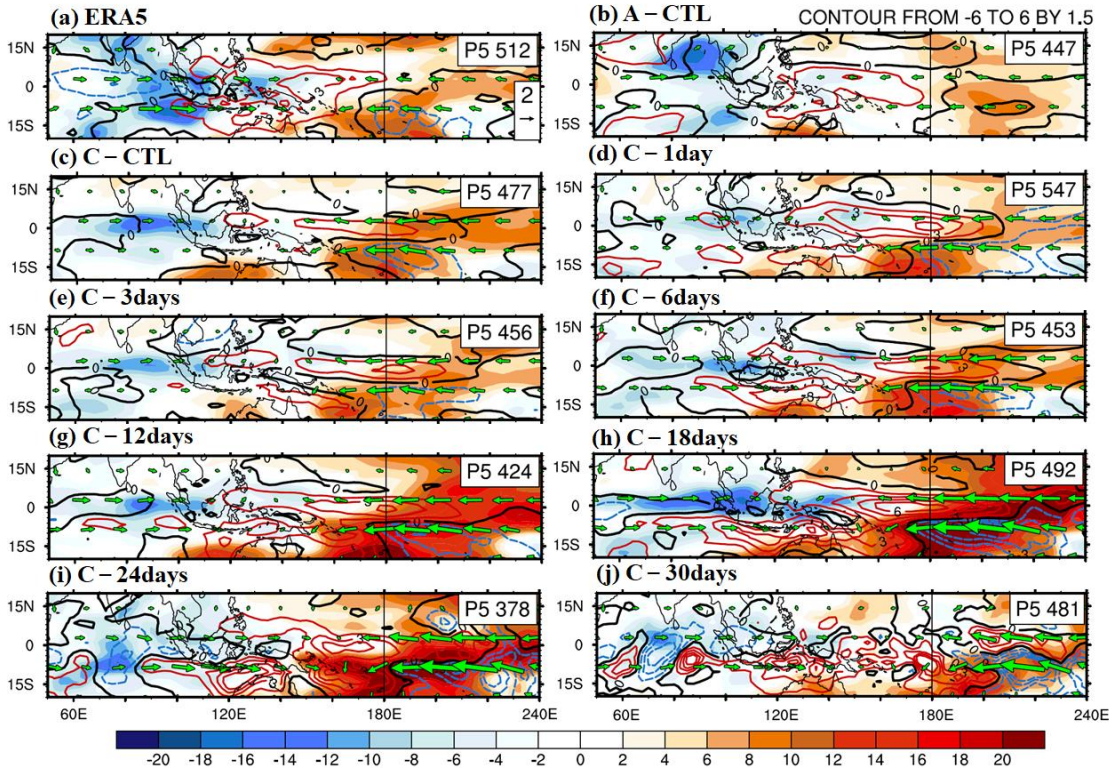

1134

1135 **Figure 10.** Filtered the column-integrated MSE tendency (J kg−1 s−1, shading),
1136 precipitation (mm d−1, contours interval 1.5) and 850-hPa wind (green vector,
1137 reference vector 2 m s−1) in phase 5: (a) ERA5, (b) A−CTL, (c) C−CTL, (d) C−1day,
1138 (e) C−3days, (f) C−6days, (g) C−12days, (h) C−18days, (i) C−24days, and (i)
1139 C−30days. Solid-red, dashed-blue, and thick-black curves represent positive, negative,
1140 and zero values, respectively.

1141

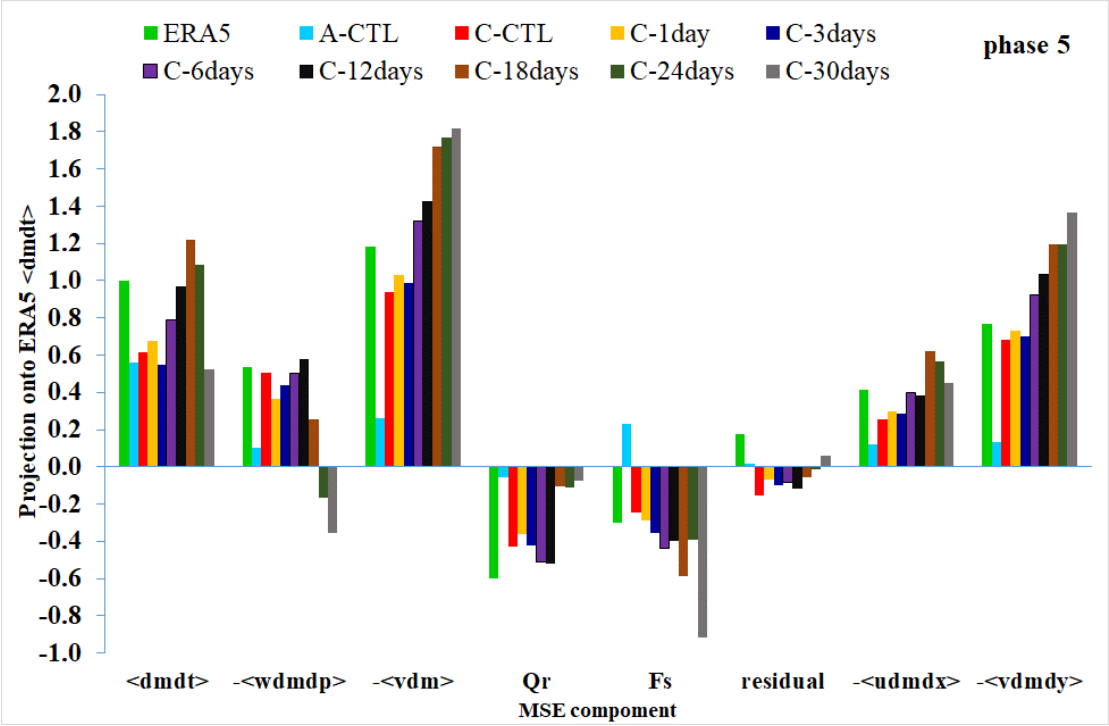

Figure 11. The projection of each MSE component onto the ERA5 column-integrated MSE tendency at phase 5 over the MC (20° S–20° N, 90–210° E): <dmdt>, -<wdmdp>, -<vdm>, Qr, Fs, and residual; decomposition of horizontal MSE advection to zonal and meridional advection (-<udmdt> and -<vdmdy>).

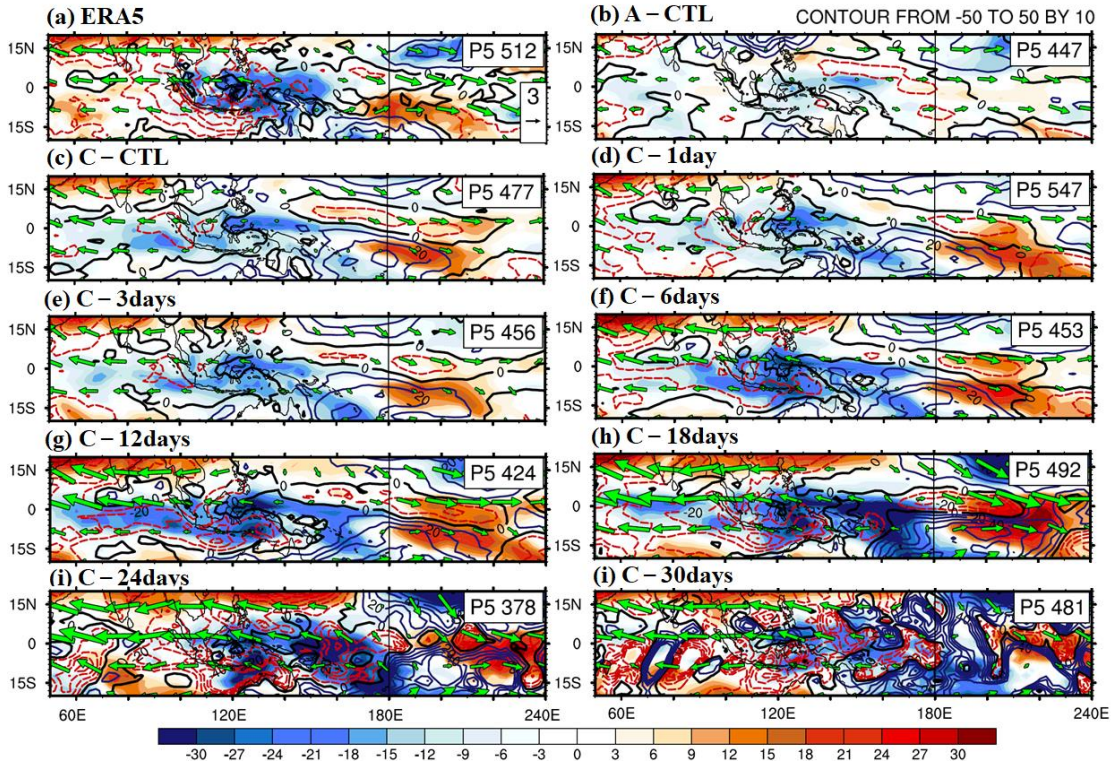

Figure 12. Filtered column-integrated vertical (J kg−1 s−1, shading) and horizontal MSE advection (J kg−1 s−1, contours interval 6.0), and 200-hPa wind (green vector with reference vector 3 m s−1): (a) ERA5, (b) A−CTL, (c) C−CTL, (d) C−1day, (e) C−3days, (f) C−6days, (g) C−12days, (h) C−18days, (i) C−24days, and (j) C−30days. Solid-blue, dashed-red, and thick-black curves represent positive, negative, and zero values, respectively.

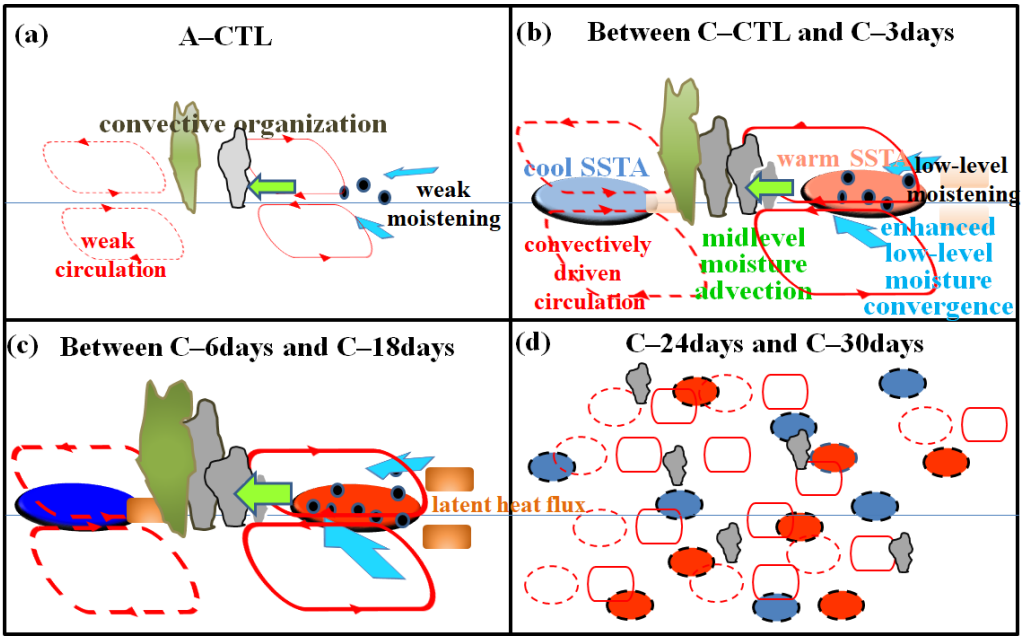

Figure 13. Schematic diagrams illustrate the anomalous circulation and moistening processes during the eastward propagation of the MJO in experiments: (a) A−CTL, (b) high-frequency SST feedback experiments (C−CTL, C−1day, and C−3days), (c) low-frequency SST feedback experiments (C−6days, C−12days, and C−18days), and (d) C−24days and C−30days experiment. In each panel, the horizontal line represents the equator. The size of clustering gray clouds indicates the strength of convective organization. A red ellipse indicates convection-driven circulation. In the coupled simulations, light red (blue) filled ovals represent warm (cold) SST anomalies, respectively, and grass green filled rectangle represent latent heat flux. Unresolved convective processes are indicated by black dots representing low-level moisture convergence. Low-level moisture convergence into the equatorial trough is shown by light blue arrows, while midlevel moisture advection is represented by left-pointing green arrows. The deeper colors or thicker lines on the map indicate stronger anomalies of the MJO perturbations. Note: The concept of the figure is based on DeMott et al. (2014).